Proton induced reactions and the astrophysical p process

Ph.D. Thesis

Gábor Gyula Kiss

Supervisor:
Endre Somorjai

Consultant:
György Gyürky

University of Debrecen
and
Institute of Nuclear Research of the Hungarian Academy of Sciences
(ATOMKI)

Debrecen, 2008

Ezen értekezést a Debreceni Egyetem TTK Fizika Doktori Iskola
Magfizika programja keretében készítettem a
Debreceni Egyetem TTK doktori (PhD) fokozatának elnyerése céljából.

Debrecen, 2008. július 25. Kiss Gábor Gyula

Tanúsítom, hogy Kiss Gábor Gyula doktorjelölt 2005-2008 között
a fent megnevezett Doktori Iskola Magfizika
programjának keretében irányításommal végezte munkáját.
Az értekezésben foglalt eredményekhez a jelölt önálló alkotó
tevékenységével meghatározóan hozzájárult.
Az értekezés elfogadását javaslom.

Debrecen, 2008. július 25. Dr. Somorjai Endre
témavezető

Contents

1 Introduction **5**

2 Characteristic astrophysical quantities **9**

2.1 Reaction rate 9

2.1.1 Neutron-induced reactions 10

2.1.2 Gamma-induced reactions 11

2.2 Reaction rate for charged particle-induced reactions 12

2.3 The astrophysical S factor 13

2.4 The Gamow window 14

3 Synthesis of the heavy elements **17**

3.1 Neutron capture processes 17

3.1.1 The s process 20

3.1.2 The r process 22

3.2 The p process 23

3.2.1 The p nuclei 23

3.2.2 The synthesis of the p nuclei 25

3.2.3 Statistical model calculations 26

3.2.4 Experimental investigation of the astrophysical p process 27

4 Proton induced cross section measurements on Germanium isotopes **31**

4.1 Introduction 31

4.1.1 Measuring the cross section of proton-induced reactions 32

4.2 Proton induced reactions on Germanium isotopes 34
4.2.1 Investigated reactions 36
4.2.2 Target preparation 37
4.2.3 Irradiations 39
4.2.4 Gamma-counting 41
4.2.5 Experimental results 45
4.3 Discussion and conclusions 49
4.4 Summary 56

5 The cross section measurement of the ^{85}Rb(p,n)^{85}Sr reaction 57
5.1 Introduction 57
5.2 The ^{85}Rb(p,n)^{85}Sr reaction 58
5.2.1 Feature of the investigated reaction 58
5.2.2 Target preparation and target-thickness determination 59
5.2.3 Irradiation 63
5.2.4 Gamma-counting and results 64
5.3 Conclusions 69
5.4 Summary 73

6 Proton capture cross sections of ^{106,108}Cd isotopes 75
6.1 Introduction 75
6.2 Investigation of (p,γ) reactions on Cd isotopes 75
6.2.1 Target production and irradiation 78
6.2.2 Gamma-counting and results 80
6.3 Conclusions 84
6.4 Summary 88

7 Summary 89

8 Összefoglalás 93

9 Publications 105

1 Chapter

Introduction

Why are stars shining? What is the origin of the chemical elements? These questions remained mainly unanswered until 1957, when E. M. Burbidge, G. R. Burbidge, W. A. Fowler, F. Hoyle [1] and A. Cameron [2] almost simultaneously summarized the existing knowledge of the burning processes of stars explaining the origin of the chemical elements. From their work, a new interdisciplinary branch of physics — Nuclear Astrophysics — was born.

The recognition of the role of nuclear reactions in the energy production of stars started in the beginning of the 20th century with the work of E. Rutherford, who recognized that nuclei store enormous amount of energy. The next step was done a decade later by G. Gamow with the prediction of the quantum mechanical tunneling effect [3] which makes possible the nuclear reaction to occur at lower energies than the Coulomb barrier. At the end of the 40's, R. A. Alpher, H. A. Bethe and G. Gamow recognized the relationship between the neutron capture cross section of the heavy elements and their isotopic abundance [4]. The survey of the emission spectrum of the stars proved that the nucleosynthesis occurs even nowadays, since the γ-rays of ^{98}Tc were found and this isotope has a half-life of only 4 million years. Later, the emission lines of other isotopes with even shorter half-lives were found (e.g. ^{26}Al [5]).

In 1957 E. M. Burbidge, G. R. Burbidge, W. A. Fowler and F. Hoyle created the first comprehensive theory of the burning mechanism of the stars and their role in the nucleosynthesis. The origin of almost all stable isotopes was explained assuming eight main synthesizing processes:

- The Hydrogen burning phase is responsible for converting protons to Helium.

- Starting with the triple α process, the Helium burning phase is creating ^{12}C which is the fourth most abundant isotope. A part of the produced ^{12}C is consumed via the $^{12}\mathrm{C}(\alpha,\gamma)^{16}\mathrm{O}$ reaction.

- It was suggested that further α captures could extend nucleosynthesis beyond ^{16}O to ^{20}Ne, ^{24}Mg, etc., up to the very stable, double magic nucleus, ^{40}Ca in the so called α process. However, after the experiments showed that the rate of $^{16}\mathrm{O}(\alpha,\gamma)^{20}\mathrm{Ne}$ reaction is very slow at stellar energies, it became evident that Carbon and Oxygen burning are responsible for the origin of species from Neon to Sulphur.

- A hypothetical e process contains a group of nuclear reactions by which the iron group is assumed to be synthesized. At temperatures ≥ 5 x 10^9 K and densities ≥ 3 x 10^6 g cm^{-3} there are great numbers of collisions between high-energy photons and nuclei. These collisions break up the nuclei and the fragments of promptly combine with other particles. The e-process (the e stands for equilibrium) is presumed to occur in a supernova explosion.

- It was proposed, that beyond the Iron region — where the binding energy per nucleon reaches its maximum — the chemical elements are produced in series of neutron capture in the so-called s process

- From the analysis of the abundance curve of the chemical elements it was obvious that another neutron capture process must exist, where the neutron capture rate is much higher than the β-decay rate of the produced isotopes. This process was named as r process

- The so-called p process is the one to be responsible for the production of the heavy, proton rich nuclei like ^{106}Cd with series of proton capture reactions. At the end of the 70's this picture changed. It was shown that in the synthesis of the *p* nuclei, photodisintegration reactions are playing a key role [6].

- Finally, the *x* process is building up the light isotopes like Deuteron, Lithium, Beryllium and Boron.

As soon the accuracy of the abundance distribution of the chemical elements and their isotopes and the nuclear physics inputs used in the calculations increased, it became necessary to improve the descriptions of the different astrophysical processes and revise the astrophysical scenario in which they occur [7]. Some parts of the puzzle are still missing like the astrophysical site where the *r* process takes place.

Also in the case of the production of the *p* nuclei there are still open questions. The aim of my work is to contribute to a more complete reaction *p* process network calculation with providing experimental proton-induced reaction rates. In the second Chapter the necessary astrophysical quantities are introduced. Since the *p* process involves photodisintegration reactions on already produced *s* and *r* seed nuclei, a short overview of the neutron capture processes as well as the *p* process are given in Chapter 3. The motivation, the experimental approch, the results and conclusions on the cross section measurements of the ^{70}Ge(p,γ)^{71}As, ^{76}Ge(p,n)^{76}As reactions can be found in Chapter 4 and the details of the cross section measurement of the ^{85}Rb(p,n)^{85}Sr reaction and the conclusions on this experiment can be found in Chapter 5. In Chapter 6 the cross section measurement of proton capture reactions on ^{106,108}Cd *p* isotopes are presented. At the end of my dissertation I summarize the results in English (Chapter 7) and in Hungarian (Chapter 8).

2 Chapter

Characteristic astrophysical quantities

The cross sections derived in the present work are used as input for astrophysical calculations, therefore it is necessary to introduce the most important astrophysical quantities first. In the following the reaction rate, the probability of tunneling through the Coulomb barrier at astrophysical energies and the astrophysical S factor will be defined. Moreover, it will be demonstrated that the multiplication of the Maxwell-Boltzmann velocity distribution describing the velocity of the interacting nuclei and the probability of the tunneling effect together form the so-called Gamow peak, where the nuclear reactions between charged particles can occur in stars. This chapter is strongly based on the textbooks [8, 9].

2.1 Reaction rate

In normal stellar matter the nondegenerated gas is in thermal equilibrium. The nuclei are moving nonrelativistically, their velocity distribution can be described by the well-known Maxwell-Boltzmann distribution:

$$\phi(v) = 4\pi v^2 \left(\frac{m}{2\pi kT}\right)^2 \exp\left(-\frac{\mathrm{m}v^2}{2\mathrm{kT}}\right). \tag{2.1}$$

The $\langle \sigma \upsilon \rangle$ reaction rate for interacting x + y nuclei can be written as

$$\langle \sigma \upsilon \rangle = \int_0^\infty \int_0^\infty \phi(\upsilon_x)\phi(\upsilon_y)\sigma(\upsilon)\upsilon d\upsilon_x d\upsilon_y, \tag{2.2}$$

where υ represents the relative velocity between the x and y nuclei. Using the definition of the reduced mass:

$$\mu = \frac{m_x m_y}{m_x + m_y}, \tag{2.3}$$

the $\langle \sigma \upsilon \rangle$ can be written as

$$\langle \sigma \upsilon \rangle = 4\pi \left(\frac{\mu}{2\pi kT} \right)^{3/2} \int_0^\infty \upsilon^3 \sigma(\upsilon) \mathrm{exp} \left(-\frac{\mu \upsilon^2}{2\mathrm{kT}} \right) \mathrm{d}\upsilon. \tag{2.4}$$

Substituting the center-off-mass energy E = 1/2 $\mu \upsilon^2$, the $\langle \sigma \upsilon \rangle$ reaction rate per particle pair has the following form:

$$\langle \sigma \upsilon \rangle = \left(\frac{8}{\pi \mu} \right)^{1/2} \frac{1}{(kT)^{3/2}} \int_0^\infty \sigma(E) E \mathrm{exp} \left(-\frac{\mathrm{E}}{\mathrm{kT}} \right) \mathrm{dE}. \tag{2.5}$$

It can be seen that the reaction rate depends on the σ(E) cross section. Since in the nucleosynthesis charged particle-, neutron- and γ-induced reactions are playing a role, the characteristics of the different types of reactions will be described as follows

2.1.1 Neutron-induced reactions

The abundance of *s* and *r* seed nuclei — produced via neutron capture, see Chapter 3 — are important for the *p* process model calculations, therefore, I define the $\langle \sigma \upsilon \rangle$ reaction rate for non-resonant neutron-induced reactions. The neutrons produced in several astrophysical reactions are quickly thermalized in stars. Their velocity distribution can also be described by the Maxwell-Boltzmann expression. The neutron-induced reactions are taking place most probably at the maximum of the velocity distribution, at E_T = kT energies. At low energies the

$$\sigma_l \propto \left(\frac{1}{\upsilon^2}\right)\Gamma_l, \tag{2.6}$$

expression can be used. The Γ_l partial width can be written as

$$\Gamma_l \propto (\upsilon R)^{2l+1} \propto E^{l+1/2} \tag{2.7}$$

where R and l are the channel radius and the orbital angular momentum, respectively. Accordingly, the $\langle\sigma\upsilon\rangle$ reaction rate per particle pair is:

$$\langle\sigma\upsilon\rangle \propto \int_0^\infty E^{l+1/2}\mathrm{exp}\left(-\frac{\mathrm{E}}{\mathrm{kT}}\right)\mathrm{dE}. \tag{2.8}$$

Most of the non-resonant neutron-induced reactions takes place in the stellar energy window, represented by the $E^{l+1/2}exp\left(-\frac{E}{kT}\right)$ integrand. Since, compared to the Coulomb barrier, the influence of the centripetal barrier on the reaction rates is far smaller, this effective energy region can be estimated by using the Maxwell-Boltzmann velocity distribution.

2.1.2 Gamma-induced reactions

In the production of the *p* nuclei photodisintegration reactions are playing key role (for details see Chapter 3). For this reason, here the characteristics of the γ-induced reactions are presented.

The energy density of the electromagnetic waves at T temperature with frequencies between ν and $d\nu$ is given by Planck radiation law

$$u(\nu)d\nu = \frac{8\pi h\nu^3}{c^3}\frac{1}{e^{h\nu/kT}-1}d\nu \tag{2.9}$$

This can be written — by substituting $\mathrm{E}_\gamma = \mathrm{h}\nu$ — as

$$u(\nu)d\nu = \frac{8\pi}{(hc)^3}\frac{E_\gamma^3}{e^{E_\gamma/kT}-1}dE_\gamma. \tag{2.10}$$

The number of photons at T temperature with energies between E_γ and dE_γ per unit volume is

$$N_\gamma(E_\gamma)dE_\gamma = \frac{8\pi}{(hc)^3}\frac{E_\gamma^2}{e^{E_\gamma/kT}-1}dE_\gamma \tag{2.11}$$

and the photodisintegration decay constant (probability of decay per nucleus per second) at a given T temperature

$$\lambda_\gamma = \frac{8\pi}{h^3c^2}\int_0^\infty \frac{E_\gamma^2}{e^{E_\gamma/kT}-1}\sigma(E_\gamma)dE_\gamma \tag{2.12}$$

Since most of the photodisintegration reactions have negative Q value, the lower limit of the integration is determined by the threshold energy.

2.2 Reaction rate for charged particle-induced reactions

The velocity averaged cross section, the reaction rate for charged particles are determined by the Maxwell-Boltzmann velocity distribution and the probability of tunneling through the Coulomb barrier.

The height of the Coulomb barrier is orders of magnitude higher than the energy of the interacting charged particles during the non-explosive nucleosythesis. Therefore the nuclear reactions can occur only with tunneling effect. In quantum mechanics the $|\Psi(\vec{r})|^2$ quantity refers to the probability of finding the particle at position $\vec{r}$. The probability of penetrating the Coulomb barrier via tunneling effect is

$$P = \frac{\left|\Psi(\vec{R_n})\right|^2}{\left|\Psi(\vec{R_c})\right|^2}, \tag{2.13}$$

where $\vec{R_c}$ is the so-called classical turning point (from classical point of view, this is the minimum distance between the target and the incident nucleus) and $\vec{R_n}$ is the nuclear radius. At low energies where E $\ll$ E$_c$ (equivalently, where $\left|\vec{R_c}\right| \gg \left|\vec{R_n}\right|$) this probability can be approximated with (using s wave approximation, i.e. only $l = 0$ waves are taken into account)

$$P = \exp(-2\pi\eta), \tag{2.14}$$

where η is the Sommerfeld parameter,

$$\eta = \frac{Z_x Z_y e^2}{\hbar \nu}. \tag{2.15}$$

In practice the Gamow factor

$$2\pi\eta = 31.29105712 Z_x Z_y \left(\frac{\mu}{E}\right)^{1/2}, \tag{2.16}$$

is used, where the center-of-mass energy E should be given in keV and μ in amu.

2.3 The astrophysical S factor

The charged particle cross sections drop rapidly for energies below the Coulomb barrier because the probability of the tunneling effect decreases exponentially

$$\sigma(E) \propto \exp(-2\pi\eta). \tag{2.17}$$

Therefore, in several cases the experiments can be performed at higher energies and then the results are extrapolated into lower energy regions of astrophysical interest. However, the strong energy dependence of the cross section makes this extrapolation difficult.

For extrapolation, in the case of non-resonant reactions instead of the cross section, the much less energy dependent quantity

$$S(E) = \frac{\sigma(E) E}{\exp(-2\pi\eta)}, \tag{2.18}$$

is used. This is the so-called astrophysical S factor. Inserting the definition of S(E) into equation 2.5 for reaction rate per particle pairs $\langle \sigma v \rangle$ one obtains

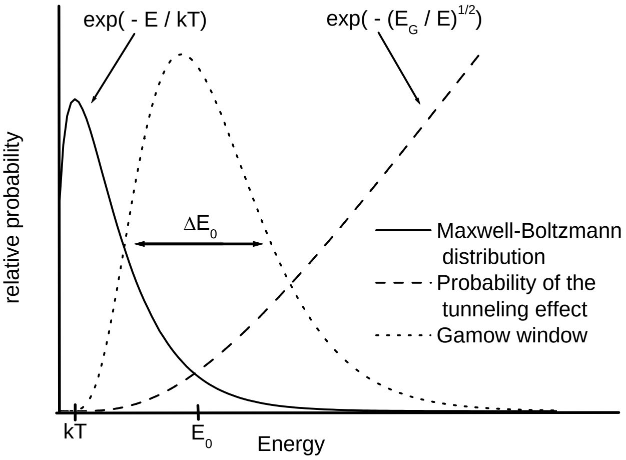

2.1. Figure: The Maxwell-Boltzmann distribution and the quantum mechanical probability of the tunneling effect are shown. The folding of the velocity distribution by the tunneling probability results in the so-called Gamow window (strongly enlarged in the figure), where the nuclear reactions occur in stars.

$$\langle \sigma v \rangle = \left(\frac{8}{\pi\mu}\right)^{1/2} \frac{1}{(kT)^{3/2}} \int_0^\infty S(E)\mathrm{exp}\left(-\frac{\mathrm{E}}{\mathrm{kT}} - \frac{\mathrm{b}}{\mathrm{E}^{1/2}}\right) \mathrm{dE}, \tag{2.19}$$

where b corresponds to the barrier penetrability and can be written as

$$b = (2\mu)^{1/2}\pi e^2 Z_x Z_y/\hbar = 0.989 Z_x Z_y \mu^{1/2}[MeV]^{1/2}. \tag{2.20}$$

The quantity b^2 is called Gamow energy.

2.4 The Gamow window

The Coulomb penetration probability folded with the Maxwell-Boltzmann velocity distribution forms the so-called Gamow peak. These functions as well as the Gamow window is presented in Fig. 2.1. The considerations here are limited for low energy direct captures (where resonances are not taking place) and for high energy compound reactions (where the resonances are overlapping) when the cross section varies smoothly with the energy. For a given stellar environment, the charged particle-induced nuclear reactions are taking place in this relatively narrow energy window around the E_0 effective burning energy:

$$E_0 = \left(\frac{bkT}{2}\right)^{\frac{2}{3}}. \tag{2.21}$$

This means that with increasing stellar temperature and charge numbers the Gamow peak is shifted toward higher energies. Typically, the E_0 is too low for direct cross section measurements.

The main challenge in nuclear astrophysics is to derive the cross sections in the Gamow window or as close to it as possible. In Chapter 4, 5 and 6 the cross section measurements, the results of proton-induced reaction on Germanium, Rubidium and Cadmium isotopes in the astrophysically relevant energy region are presented for the *p* process.

3 Chapter

Synthesis of the heavy elements

3.1 Neutron capture processes

It is well known that below the so-called iron-peak the chemical elements in stars are built up by consecutive burning phases via charged particle reactions [1, 2, 7-9] The height of the Coulomb barrier is increasing drastically with the increasing charge number of the participants of the thermonuclear reactions. Therefore, above Iron these cross sections are far to small to explain the observed abundance of the chemical elements [10] shown in Fig. 3.1. Furthermore, the binding energy per nucleon reaches its maximum in the Iron-Nickel region. Consequently, the processes synthesizing the heavy elements are not producing but consuming energy from the star.

According to these facts, the main nuclear reactions building up the bulk of the heavy elements are neutron capture and β-decay [1, 2, 7]. The abundance distribution suggests the existence of two main neutron capture processes. In the following I describe these processes. A schematic representation of the different reaction paths are demonstrated in Fig. 3.3.

Before discussing the different processes synthesizing the heavy elements, an overview on the life of a typical massive star is given. Stars are formed from interstellar gas clouds. At first, the internal heat resulting from the gravitational contraction is radiated away. Since the opacity is increasing

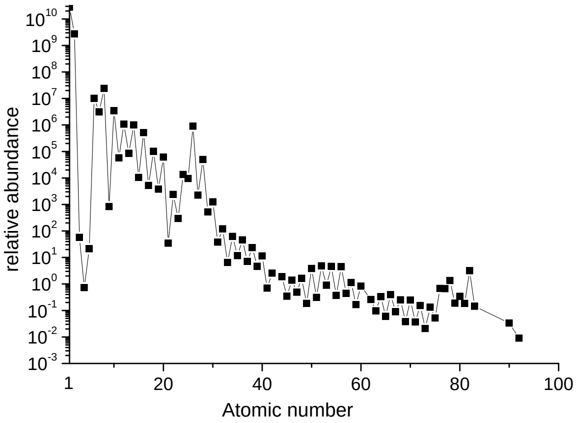

3.1. Figure: Relative abundance of the chemical elements in the solar system normalized to the abundance of Silicon (Si = 10^6). The data are taken from [10].

as the gas become denser, the energy released in the collapse can be stored. As the temperature at the center reaches about 10^7 K, thermonuclear fusion reactions — initiating with the so-called hydrogen burning — start to take place. The gravitional contraction is temporary halted because there is an equilibrium between the gravitional force and the outward pressure: the size, the temperature and the luminosity of the star becomes stable. When the hydrogen fuel is exhausted, the outward pressure against the gravity is no longer sustained by nuclear reactions. The core begins to collapse, increasing its temperature and pressure which becomes great enough — if the mass of the star is sufficiently high — to ignite the helium and start a helium-to-carbon fusion, creating sufficient outward pressure to halt the collapse again. This cycle is repeated several times. Each time the core collapses and the collapse is halted by the ignition of a further fuel producing higher temperatures, pressures and more massive nuclei in the core. The star becomes like an onion since the previous burning processes are also taking place in outer layers of the star, where the density and the temperature is lower than in the core but still sufficiently high — as can be seen in

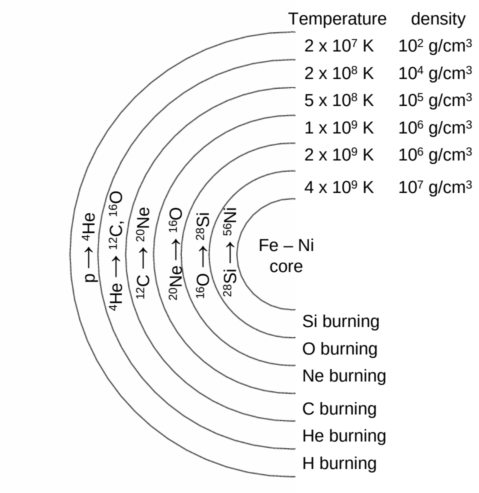

3.2. Figure: Schematic view of a massive star before the supernova explosion. The synthesizing processes as well as the typical temperatures and densities of the layers are indicated.

Fig 3.2. However, each successive burning stage generates less energy and shorter duration than the previous one. When the core contains mainly the elements of the Iron group, further thermonuclear reactions cannot occur since the binding energy per nucleon reached its maximum [8, 9].

At this point, the necessary outward pressure standing against the gravity can be produced through the degeneracy of the electrons in the core. However, if the star is massive enough, the Iron-Nickel core will exceed the Chandrasekhar limit ($1.38 M_\odot$), at which point this mechanism fails. In a typical Type II core-collapse supernova, the core implodes due to its own mass, and nothing can prevent the collapse. The temperature and the density increase rapidly, electrons and protons merge via electron capture, producing neutrons and neutrinos. Much of the heat of the core is carried away by the neutrinos, accelerating the collapse. When the density of the inner core is comparable to that of an atomic nucleus, further collapse is stopped by the strong force and the infalling material rebounds, producing a shock wave [8, 9]. The star explodes as a supernova.

It have to be noted that there are other types of supernovae — the so-called type I.a (binary system), type I.b and I.c (massive stars running out of fuel, however, the progenitors of Types Ib and Ic have lost most of their outer envelopes due to strong stellar winds or from interaction with a companion). From the observation point of view, the main difference between Type I and II supernova, that the core-collapse supernova contains Hydrogen, which can be seen in the emission spectra while in the emission spectra of a Type I supernova Hydrogen lines are not observable.

3.1.1 The *s* process

It is commonly accepted that the *s* process takes place in the Helium-burning phase of an AGB star (Asymptotic Giant Branch star) at typical temperatures of T $\approx$ 1-3 10^8 K [9, 11]. There are two main reactions providing a neutron density of about 10^8 neutron/cm^3, the ^{13}C(α,n)^{16}O and the ^{22}Ne(α,n)^{25}Mg. Since the neutron capture rate and the decay rate of the produced β-unstable nuclei are comparable, the *s* process path remains close to the valley of stability as it is shown in Fig. 3.3.

The standard *s* process models are underpredicting the abundance of A $\leq$ 90 *s* nuclei. In order to describe properly the observed *s* abundances, theoretical investigations suggest that two different *s* processes exist, the main or strong and the so-called weak *s* process [12, 13]. The main difference between these processes is the duration of the processes, which is about ten thousand years in the case of the main and few hundred years for the weak *s* process. Furthermore, the main *s* process takes place in AGB stars and the weak *s* process component is assigned to helium burning in massive stars [13]. Experimental investigations with measuring (n,γ) cross sections and stellar β decay rates to reconstruct properly the *s* process path are in progress [7 (and references therein)].

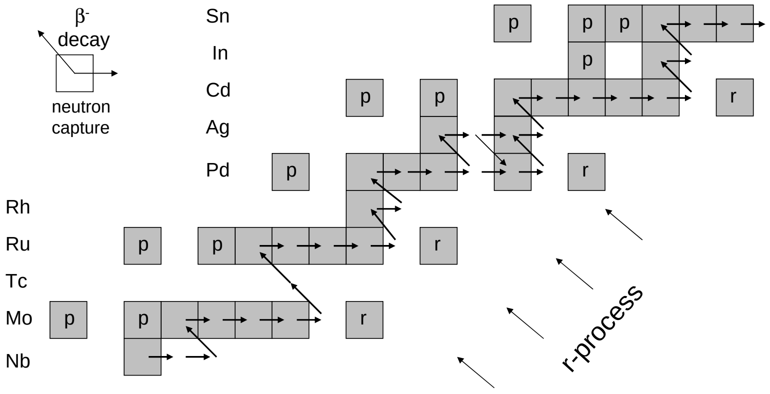

3.3. Figure: Schematic representation of nucleosynthesis in the region from Nb to Sn. The *s* process — marked with solid arrows — is synthesizing the elements near the bottom of the valley of stability. With (n,γ) reactions an unstable nucleus is produced and it decays back to the valley of stability. In the case of the *r* process, the neutron flux is much higher, the process takes place close to the neutron drip line. After the neutron flux disappears, the produced nuclei are moving toward the valley of stability with series of β^- decays, as it is indicated. The stable r-only isotopes are marked with "r". There are a few stable isotopes which cannot be produced via neutron capture. These are the so-called *p* nuclei, marked with "p".

3.1.2 The *r* process

In the fine structure of the abundance curve of the heavy elements, four peaks around A = 130, 138, 195 and 208 are observable. As it was shown previously, the *s* process remains close to the valley of stability, the existence of A = 138 and A = 208 peaks can be explained in the framework of the *s* process with shell-closure effects. However, the existence of the other two peaks around A = 130 and A = 195 cannot be explained using the *s* process models alone. Moreover, the long-lived radioisotopes — for example ^{232}Th, ^{235,238}U — are far heavier than the endpoint nuclei of the *s* process [12]. These facts provide clear evidence, that another neutron capture — the so called *r* process — must exist [1, 2, 7].

The astrophysical site of the *r* process is still under discussion [14-17]. It is clear that the neutron flux must be orders of magnitude higher than the one in the *s* process. Most probably this process takes place in the explosion of a type II supernova — where the typical neutron density is $\approx 10^{20}$ neutron/cm^3 and the temperature is around 3 GK. At such high neutron flux a series of (n,γ) reactions can produce nuclei close to the neutron drip line. At a certain point the neutron capture and the photodisintegration reactions find their equilibrium. These locations are the so-called waiting point nuclei. As soon the neutron flux disappears, these nuclei decay back into the region of the valley of stability. In Fig 3.3 neutron rich isotopes produced via the *r* process are also shown. These r-only isotopes are indicated by "r".

To describe the *r* process path the knowledge of nuclear properties — masses, neutron-capture Q values, β^--decay half lives — close to the neutron drip line are needed [18]. In the close future it will be possible to measure these values with radioactive ion beams [19].

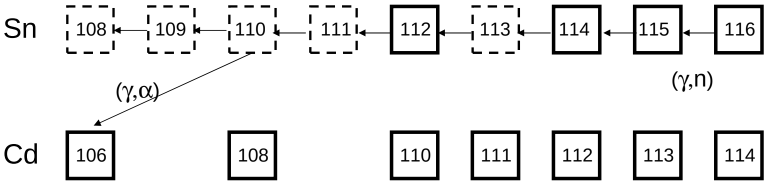

3.4. Figure: Possible reaction path synthesizing the ^{106}Cd *p* nucleus. The main role is played by a chain of (γ,n) photodisintegrations followed by (γ, α) reactions [21].

3.2 The *p* process

Most of the elements heavier than iron are built up via neutron capture in the *s* and/or *r* processes. There are, however, 35 nuclei on the proton-rich side of the valley of stability, which cannot be produced by neutron capture, because the path of these processes are blocked by stable isotopes. In the following an overview is given about these nuclei — the so-called *p* nuclei (see e.g. Fig. 3.3) — and their synthesis, the *p* process.

3.2.1 The *p* nuclei

The stable neutron-deficient nuclei with mass number of $74 \leq \mathrm{A} \leq 196$ (between ^{74}Se and ^{196}Hg) not produced via the *s* or *r* processes are the *p* nuclei [20]. Table 3.1 lists the 35 *p* nuclei with their atomic number, isotopic abundance and solar system abundance. Almost all of them are even-even except ^{113}In, ^{115}Sn, ^{138}La and ^{180}Ta, but their abundances are considerably lower. The isotopic abundances of the *p* isotopes (typically 1-0.1%) are much lower, than the other isotopes of the same element. Exceptions are the ^{92,94}Mo and ^{96}Ru where the number of seed nuclei is not sufficient to produce their high abundances. It is generally accepted that the much more abundant *s* and *r* isotopes serve as seed nuclei for the *p* process.

3.1. Table: List of the 35 so-called p nuclei taken from [9]. The abundance of ^{180}Ta and ^{180}W comes from a weak contribution of the s process, too [11]. Solar system abundances normalized to Silicon atoms (Si $= 10^6$) are also indicated. Taken from [10].

Nucleus	Z	Solar system abundance (Si $= 10^6$)	Isotopic abundance (%)	Nucleus	Z	Solar system abundance (Si $= 10^6$)	Isotopic abundance (%)
^{74}Se	34	$5.5 \cdot 10^{-1}$	0.88	^{132}Ba	56	$4.53 \cdot 10^{-3}$	0.1
^{78}Kr	36	$1.53 \cdot 10^{-1}$	0.34	^{138}La	57	$4.09 \cdot 10^{-4}$	0.09
^{84}Sr	38	$1.32 \cdot 10^{-1}$	0.56	^{136}Ce	58	$2.16 \cdot 10^{-3}$	0.19
^{92}Mo	42	$3.78 \cdot 10^{-1}$	14.84	^{138}Ce	58	$2.84 \cdot 10^{-3}$	0.25
^{94}Mo	42	$2.36 \cdot 10^{-1}$	9.25	^{144}Sm	62	$8.0 \cdot 10^{-3}$	3.1
^{96}Ru	44	$1.03 \cdot 10^{-1}$	5.52	^{152}Gd	64	$6.6 \cdot 10^{-4}$	0.2
^{98}Ru	44	$3.50 \cdot 10^{-2}$	1.88	^{156}Dy	66	$2.21 \cdot 10^{-4}$	0.06
^{102}Pd	46	$1.42 \cdot 10^{-2}$	1.02	^{158}Dy	66	$3.78 \cdot 10^{-4}$	0.10
^{106}Cd	48	$2.01 \cdot 10^{-2}$	1.25	^{162}Er	68	$3.51 \cdot 10^{-4}$	0.14
^{108}Cd	48	$1.43 \cdot 10^{-2}$	0.89	^{164}Er	68	$4.04 \cdot 10^{-3}$	1.61
^{113}In	49	$7.9 \cdot 10^{-3}$	4.3	^{168}Yb	70	$3.22 \cdot 10^{-4}$	0.13
^{112}Sn	50	$3.72 \cdot 10^{-2}$	0.97	^{174}Hf	72	$2.49 \cdot 10^{-4}$	0.16
^{114}Sn	50	$2.52 \cdot 10^{-2}$	0.66	^{180}Ta	73	$2.48 \cdot 10^{-6}$	0.01
^{115}Sn	50	$1.29 \cdot 10^{-2}$	0.34	^{180}W	74	$1.73 \cdot 10^{-4}$	0.13
^{120}Te	52	$4.3 \cdot 10^{-3}$	0.09	^{184}Os	76	$1.22 \cdot 10^{-4}$	0.02
^{124}Xe	54	$5.71 \cdot 10^{-3}$	0.12	^{190}Pt	78	$1.7 \cdot 10^{-4}$	0.01
^{126}Xe	54	$5.09 \cdot 10^{-3}$	0.11	^{196}Hg	80	$5.2 \cdot 10^{-4}$	0.15
^{130}Ba	56	$4.76 \cdot 10^{-3}$	0.11				

3.2.2 The synthesis of the *p* nuclei

Most probably the *p* process takes place in the O/Ne layer of type II supernovae. When the shock wave is passing through this layer for a short time ($\approx$ 1s) it compresses and heats up this stellar region to 1.8 - 3.3 GK [20]. Theoretical investigations agree that each *p* nucleus is synthesized in a relatively narrow temperature-window: A $\leq$ 92, 92 $\leq$ A $\leq$ 144 and A$\geq$ 144 are mainly produced in stellar environments with T $\geq$ 3 GK, 2.7 $\leq$ T $\leq$ 3.0 GK and T $\leq$ 2.5 GK, respectively. At these temperatures, a series of (γ,n) photodisintegration reaction is taking place on the already produced *s* and *r* seed nuclei. As the reaction flow moves toward the more proton rich side, the energy necessary to remove a neutron from the nucleus is increasing. At the same time the proton and α-particle separation energy is decreasing. Consequently (γ,p) and (γ, α) reactions start to play a role. As an example, Fig. 3.4 shows a probable reaction path building up the ^{106}Cd *p* nucleus.

Additional processes such as the *rp* and *νp* can also give a slight contribution to the abundance of the light *p* nuclei. The *rp* process was proposed by Woosley *et al.*, [22]. This explosive nucleosynthesis scenario takes place at high temperature hydrogen-rich environment, most probably in X-ray bursts of accreting neutron stars [23]. In a series of fast radiative proton-capture reactions, nuclei close to the proton drip line can be built up and β decay back to the valley of stability. Recent work of Schatz *et al.,* [24] demonstrated that the endpoint of this process is around Z $\approx$ 54. Of course, the contribution of this process to the observed *p* abundances depends on the amount of material ejected from the X-ray bursts [20, 23].

The *νp* process involves a neutrino wind generated by the collapse of a Type II Supernova. This process could give a contribution to the abundance of the A $\geq$ 64 nuclei [25]. Moreover via neutral current $(\nu, \nu'$ N) and charged current reactions, the rarest stable odd-odd nuclei ^{138}La and ^{180}Ta can be also built up [23]. Recent theoretical investigations show that this process can explain the overproduction of ^{92,94}Mo and ^{96,98}Ru [26]. However, further investigations on the neutrino spectrum from the Type II Supernovae explosion and on neutrino-induced cross sections are needed.

3.2.3 Statistical model calculations

The modeling of the synthesis of the p nuclei and reproducing their abundances require an extended reaction network calculation involving nearly 20 000 of reactions on $\approx$ 2000 stable and unstable nuclei [20, 27, 28]. The necessary reaction rates are calculated using the Hauser-Feshbach statistical model [29]. Theoretical p process models reproduce the observed isotopic abundances of nearly 60% of the p nuclei within a factor of 3. However, there are a large number of discrepancies, for example, the p isotopes of Molybdenum, Ruthenium as well as the ^{113}In and ^{115}Sn are underpredicted by the calculations. In the following a short overview about the basis of statistical model calculations will be given.

The $\sigma^{\mu\nu}$ cross section of the reaction $i^{\mu}(j,o)m^{\nu}$ from target state i^{μ} to the excited state m^{ν} of the final nucleus with center-of-mass energy E_{ij} and reduced mass μ_{ij} can be written as:

$$\begin{aligned} \sigma^{\mu\nu}(E_{ij}) = \frac{\pi\hbar^2/(2\mu_{ij}E_{i,j})}{(2J_i^{\mu}+1)(2J_j+1)} \sum_{J,\pi}(2J+1)\times \\ \times\frac{T_j^{\mu}(E,J,\pi,E_i^{\mu},J_i^{\mu},\pi_i^{\mu})T_o^{\mu}(E,J,\pi,E_m^{\nu},J_m^{\nu},\pi_m^{\nu})}{T_{tot}(E,J,\pi)}, \end{aligned} \tag{3.1}$$

where J denotes the spin, E is the corresponding excitation energy and π is the parity of the excited states. The $T_{tot} = \sum_{\nu,o} T_o^{\nu}$ describes the transitions into all possible bound and unbound states ν in all energetically accessible exit channels o including the entrance channel i. At stellar environment the nuclei are thermally excited and the temperature dependent σ^* astrophysical cross section for the $i^{\mu}(j,o)m^{\nu}$ reaction can be written as:

$$\sigma^*(E_{ij}) = \frac{\sum_{\mu}(2J_i^{\mu}+1)\mathrm{exp}(-\mathrm{E_i^{\mu}/kT^*})\sum_{\nu}(\sigma^{\mu\nu}(\mathrm{E_{ij}}))}{\sum_{\mu}(2J_i^{\mu}+1)\mathrm{exp}(-\mathrm{E_i^{\mu}/kT^*})} \tag{3.2}$$

where T^* is the plasma temperature and k is the Boltzmann constant. The important input parameters of the statistical model calculations are the level density of the excited states and the T particle and γ-transmission coefficients. The reliability of the calculations is determined by these inputs. The level densities are usually based on theoretical works [30 (and references therein)]. The individual particle transmission coefficients are calculated from solving the Schrödinger equation with an optical potential which can be based on theoretical models or can be derived by comparing the suitable measured and calculated reaction cross sections.

The main assumption that has to be taken into account when performing statistical model calculations is that the number of levels in the compound nucleus has to be sufficiently high in the relevant energy range, which can act as doorway states to form a compound nucleus [31]. Otherwise, the application of the statistical model for a level density which is not sufficiently large results in an overestimation of the cross section. The applicability of the statistical model was investigated by Rauscher *et al.* [31] for neutron-, proton-, and α-induced reactions. As a result, a "map" with the minimum temperatures for each nucleus at which the above discussed conditions are fulfilled can be found [31]. It can be seen that farther from the valley of stability the minimum required temperatures of the calculations are increasing. These temperatures are sometimes higher than the temperatures corresponding to the synthesis of the p isotopes. Moreover, shell effects have to be also taken into account. Therefore, experimental tests of the statistical model calculations are clearly needed [9, 27, 28].

3.2.4 Experimental investigation of the astrophysical p process

According to theoretical investigations, (γ,p) reactions are playing a key role [20, 27, 28] in the production of the light p nuclei. There are two ways to determine the stellar (γ,p) reactions rates experimentally. First, it is possible to measure (γ,p) cross sections and convert the measured cross sections to stellar reaction rates. Alternatively it can be derived from the cross section of the inverse (p,γ) reaction. Here the comparison between these two methods will be presented from physical and technical point of view.

In a hot stellar environment nuclei are thermally excited. The number of thermally populated states with E_x and J^μ relative to the one at ground state, according to the Boltzmann statistics is:

$$\frac{n(E_x, J_\mu)}{n(g.s.)} = \frac{(2J_\mu + 1)e^{-E_\mu/kT}}{\sum_\mu (2j_\mu + 1)e^{-E_\mu/kT}} \tag{3.3}$$

In the following, I will discuss the (γ,p) reactions. In general, proton emission at energies below the Coulomb barrier prefers the ground state decay because of the largest tunneling probability for the highest energy. The contribution of these thermally excited states on the stellar cross section σ^* can be roughly estimated. The photon density in stars at T temperature can be given by the blackbody radiation:

$$n_\gamma(E, T) = \left(\frac{1}{\pi}\right)^2 \left(\frac{1}{\hbar c}\right)^3 \frac{E^2}{e^{(E/kT)} - 1}. \tag{3.4}$$

The ground state $\sigma^{lab}_{(\gamma,p)}$ cross section has usually only a small contribution on the stellar σ^* and reaction rate since the thermal excitation reduces the required — usually high — photon energy $E^{(\gamma,p)}_{eff}$ by E_x, this way the smaller occupation probability which scales with exp(-E_x/kT) is compensated by the higher photon density at the relevant energy required for the photodisintegration of E_x excited state. Therefore (γ,p) experiments can give a precise test of theoretical calculations only for a well-defined transition.

An alternative way for determining the (γ,p) reaction rates is to measure the inverse reaction cross section and then use the detailed balance theorem. Again in this case the contribution of the thermally excited states has to be estimated. The occupation probability scales similarly with exp(-E_x/kT), but now there is no compensation. The E_p energy necessary for the tunneling is independent from the excitation energy and therefore the contribution of the excited states to the stellar cross section σ^* and reaction rate is much smaller compared to the (γ,p) reactions.

Moreover, because of technical reasons, the γ-induced cross section measurements are currently limited to the (γ,n) channel. Photodisintegration rates can be measured with photoactivation technique using continuous bremsstrahlung [32, 33] or direct neutron-counting with quasi-monochromatic γ-rays from laser Compton backscattering [34, 35]. Since the lack of appropriate γ sources up to now it was not possible to measure Coulomb suppressed (γ, α) and (γ,p) rates [36].

The series of charged particle capture cross section measurements were started at ATOMKI in the 90's. In recent years (α,γ) reaction cross sections on ^{70}Ge, ^{96}Ru, ^{106}Cd, ^{112}Sn, and ^{144}Sm [37, 38, 21, 39, 40] were measured as well as many (p,γ) cross sections [41-53]. Pronounced disagreements between the measured and the theoretically predicted cross sections were found in some cases (see e.g. [40]). More details about the experimental investigations of proton-induced reactions can be found in Chapter 4.

These experimental (p,γ) and (α, γ) rates are playing an important role in the *p* process studies with giving a possibility for adjusting the statistical model parameters. However, the number of reactions that can be studied experimentally are limited especially in the case of the α-induced reactions where the higher Coulomb barrier results in cross sections typically well below the μbarn range in the Gamow window (e.g. in the case of ^{106}Cd(α, γ) reaction, the energy of the Gamow peak is 7.21 MeV (T = 3 GK), the width of the Gamow window is 4 MeV, at these energies the cross sections are roughly between 7.7 x 10^{-12} - 3.6 x 10^{-4} barn!).

Therefore the network calculations have to rely mostly on calculated reaction rates. One of the most important input parameters used to derive the reaction rate is the optical potential taken from global potential parameterizations. Contrary to the reasonably well understood proton optical potential, the form of the α-nucleus potential is not satisfactorily known.

The global α-nucleus optical potential parameter sets are based on phenomenological models. To give a correct description of the cross sections the potential parameters are adjusted to the experimental data. Elastic alpha scattering experiments are playing particularly important role, because from the measured angular distributions the parameters of the local α-nucleus potential can be derived and compared to the global parameters.

However, experimental charged particle induced reaction data are scarce at masses higher than iron especially at energies below the Coulomb barrier. This second fact is important because the characteristics of the potential parameters are changing dramatically around the Coulomb barrier, this way the extrapolation of the results of higher energy experiments can be misleading. To derive the optical potentials experimentally, pioneering elastic α scattering experiment on ^{144}Sm was performed at ATOMKI [54]. This work continued with a series of elastic α scattering experiments [54-59] to derive local potentials and test the existing global α-nucleus optical potential parameter sets.

In the following chapters, the details of the proton-induced reaction cross section measurements on Germanium, Rubidium and Cadmium will be presented. The experimental results as well as their consequences are also discussed. Based on our experimental results a modification of the proton optical potential used in the statistical model calculations was suggested (see Chapter 4). Moreover we proved, that — despite the negative Q value — it is possible to derive stellar reaction rate for both the (p,n) and inverse (n,p) reaction from the measured (p,n) cross sections (see Chapter 5).

4 Chapter

Proton induced cross section measurements on Germanium isotopes

4.1 Introduction

To investigate the impact of nuclear reaction rates on predicted *p* abundances, a reaction flux calculation was performed by W. Rapp *et al.*, [28] recently. This network calculation took into account more than 20 000 reactions on approximately 2000 nuclei from Hydrogen to Bismuth. Since the final *p* abundances depend sensitively on the initial seed nuclei abundances [20], in this calculation the seed abundances were kept fixed. Furthermore, the cross sections of the (n,γ) reactions building up the *s* seed nuclei are well known. To study the sensitivity of the *p* abundances on nuclear reaction rates, simulations with different sets of collectively and individually modified neutron, proton, α-capture and photodisintegration rates have been performed. The reaction flux in the case of A $\leq$ 90 *p* nuclei can be seen in Fig. 4.1.

These calculations demonstrated that not only (γ,p), but (p,n) (also their inverse) reactions on *s* or *r* seed nuclei can change strongly the abundances of the light *p* nuclei [28]. There is only limited experimental information

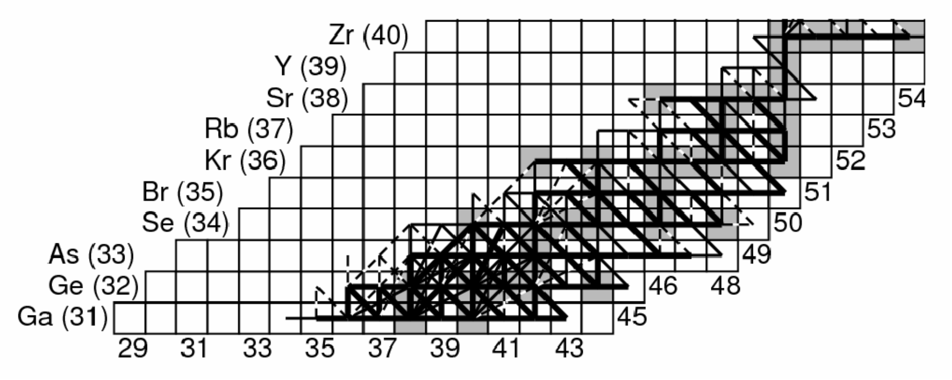

4.1. Figure: Integrated reaction flux of the *p* process in the Ga to Zr mass range during the first second of a type II SN explosion triggering a shock front in the Ne/O layer with a maximum temperature of T = 3 GK. The strength of the reaction flux is indicated by line thickness. The Figure is taken from [28].

available for the low energy cross sections of these critical (p,n) and (n,p) reactions in this mass range and the accuracy of this data is not sufficient for astrophysical applications [28]. Moreover, it is stated that some reactions — such as the ^{76}Ge(p,n)^{76}As or the ^{85}Rb(p,n)^{85}Sr — exhibit particularly strong influence on the final *p* abundances.

4.1.1 Measuring the cross section of proton-induced reactions

Before reporting on the (p,γ) and (p,n) studies done recently at ATOMKI, an overview is presented for the two, widely used methods for the cross section determination in previous experiments. Namely, the in-beam method and the activation technique is discussed.

From statistical model calculations [60] is known that the (p,γ) and (p,n) cross sections of the light *p* nuclei in the astrophysical relevant energy region are small. For example for the ^{106}Cd(p,γ) reaction is between (3 - 2000) x 10^{-6} barn, for the ^{70}Ge(p,γ) is between (30 - 7000) x 10^{-6} barn. In the case of (p,n) reactions the cross section varies typically between (1 - 300) x 10^{-5} barn.

Since all A $\leq$ 100 p nuclei are even-even, (p,γ) reactions lead to odd-even nucleus. The incident proton can be captured into several states, so in the measured in-beam γ-spectra numerous transitions are observable, which makes the analysis difficult or sometimes impossible. Moreover, if the γ-branchings of the transitions are low, the yield of the emitted γ-radiation is limited. Numerous γ-ray appears also from beam-induced reactions on impurities of the target or on backing material making the signal-to-noise ratio poor. The γ background can be suppressed using highly enriched targets, however, this way only one reaction can be studied at a time. Furthermore, the different γ-lines can correspond to transitions with different multipolarities. This way the angular distributions have to be known for each emitted γ-ray. However, the spin and parity of the levels of the compound nucleus is not always known and the precision of measuring the angular distributions are not always sufficient because of the low γ-yields. A good description for the in-beam experimental difficulties can be found in [46, 48]. These arguments also hold for (p,n) reactions, however in this case the cross sections are much higher.

The activation technique is a good alternative solution for the above mentioned experimental obstacles. Unfortunately, it can be used only if the residual nucleus of the proton-induced reaction is radioactive with reasonable half-life, roughly between 20 minutes and 1 year. Contrary to the on-line experiments, in this method the irradiation and the γ-counting are separated. The nuclei produced in the irradiation — following the β-decay — decay into the ground state with the emission of γ-radiation. The angular distribution of this γ-radiation is isotropic. Nevertheless, the low γ-branchings can limit the investigated energy region. This fact makes necessary to choose carefully the backing material and use shielding for the γ-detector to reduce the background (see below the details). Since the measured γ-spectrum is relatively simple, there is not always a need for using enriched target material, consequently it is possible to investigate several reactions parallel as it was done in the case of measuring the cross section of proton-induced reactions on Sr isotopes [45]. An important disadvantage of this method is, that — if the half-lives of the reaction products are long (several days or more) — it is necessary to use a new target for each irradiation.

Taking into account these advantages and disadvantages, it was decided to measure the cross section of the proton-induced reactions on Germanium isotopes, the ^{85}Rb(p,n)^{85}Sr and the ^{106,108}Cd(p,γ)^{107,109}In reactions using the activation technique.

4.2 Proton induced reactions on Germanium isotopes

The ^{70}Ge(p,γ)^{71}As and ^{76}Ge(p,n)^{76}As reactions are both associated to the reaction flow in this mass range as demonstrated by [28]. Figure 4.1 shows the complex reaction pattern during the first second of the shock front induced p process. Despite the astrophysical role (see below) of these reactions, cross section measurement was not carried out [61] so far. The proton capture direction gives rise to depletion of ^{70}Ge nucleus at low p process temperatures whereas the reverse reaction can produce it through a (γ,n)-(γ,p) branching at higher temperature.

The reaction ^{76}Ge(p,n)^{76}As is directly associated with the transformation of the r process seed nucleus ^{76}Ge to the p nucleus ^{74}Se in the first moments of p process nucleosynthesis; for example through the ^{76}Ge(p,n)^{76}As (γ,n)^{75}As(p,n)^{75}Se(γ,n)^{74}Se reaction chain. The cross sections of these reactions (and/or their inverse reactions) — except the ^{76}Ge(p,n)^{76}As — had been derived in several experiments and are well known [61]. Figure 4.1 suggests that many alternative reaction sequences exist, but it also underlines that during the p process ^{76}Ge is not only depleted but also produced by an initial ^{74}Ge(n,γ)^{75}Ge(n,γ)^{76}Ge reaction flux (for these (n,γ) reactions, measured cross section data are also available [61-63]. This modifies the initial

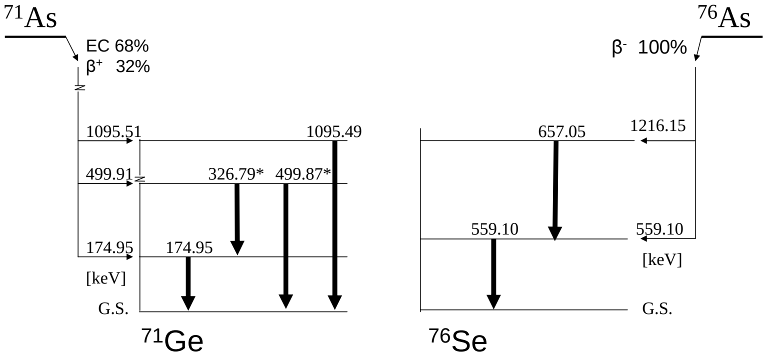

4.2. Figure: Decay scheme of ^{71}As and ^{76}As. Only the dominant transitions are indicated, these γ-rays were used for the analysis. The transitions marked with * have relative γ-intensity below 4%, therefore their statistics was not always high enough to use it in the analysis.

^{76}Ge abundance.

A detailed information of the reaction rate of ^{76}Ge(p,n)^{76}As as the sole depletion process is important to investigate the overall nucleosynthesis pattern and the history of ^{76}Ge in a type II supernova shock front environment.

The relevant energy region (the Gamow window for the (p,γ) reaction) for the investigated reactions is between 1.2 and 3.7 MeV at 1.8 - 3.3 GK stellar temperature, typical for the *p* process. The aim of the present work is to measure the cross sections inside the Gamow window. Consequently, the results can be compared with the theoretical calculations right at the astrophysically relevant energies, no extrapolation is necessary. In the following the short description of the experimental approach will be presented in Chapters 4.2.1 - 4.2.4. The results of the experiment are given in Chapter 4.2.5 and a detailed theoretical analysis of the results and their importance for the prediction of low-energy optical potential are included in Chapter 4.2.6.

4.1. Table: Proton-induced reactions on Germanium isotopes.

target	reaction	product	limitation
^{70}Ge	(p,γ)	^{71}As	no
^{70}Ge	(p,n)	^{70}As	Threshold (7.10 MeV)
^{72}Ge	(p,γ)	^{73}As	cannot be separated from ^{73}Ge(p,n)^{73}As
^{72}Ge	(p,n)	^{72}As	Threshold (5.21 MeV)
^{73}Ge	(p,γ)	^{74}As	cannot be separated from ^{74}Ge(p,n)^{74}As
^{73}Ge	(p,n)	^{73}As	cannot be separated from ^{72}Ge(p,γ)^{73}As
^{74}Ge	(p,γ)	^{75}As	product is stable
^{74}Ge	(p,n)	^{74}As	cannot be separated from ^{73}Ge(p,γ)^{74}As
^{76}Ge	(p,γ)	^{77}As	I$\gamma \leq 1.6$ %
^{76}Ge	(p,n)	^{76}As	no

4.2.1 Investigated reactions

As it was discussed previously, the activation method has the advantage to measure several cross sections simultaneously using natural targets. However, the number of reaction channels measurable with the activation method can be limited. In the following, an overview is given about the usability of this method in the case of Germanium isotopes.

The element Ge has five stable isotopes with mass numbers A=70, 72, 73, 74, and 76, having natural isotopic abundances of 20.37%, 27.31%, 7.76%, 36.73%, and 7.83%, respectively [64]. In table 4.1 a feasibility study for proton-induced reactions on Germanium isotopes using the activation technique and natural target can be found. Since the (p,n) thresholds of the ^{73,74}Ge(p,n) reactions are low, it is not possible to separate these reaction channels from the ^{72,73}Ge(p,γ) ones. The nucleus ^{75}As is stable, for this reason it is impossible to measure the cross sections of the ^{74}Ge(p,γ)^{75}As reaction. In the case of the ^{76}Ge(p,γ)^{77}As reaction the γ-intensity from the decay of the final nucleus is very low. Since for the ^{70,72}Ge(p,n) reactions the threshold is 7.10 and 5.21 MeV [64], respectively, these reactions are not

4.2. Table: Decay parameters of ^{70}Ge(p,γ)^{71}As and ^{76}Ge(p,n)^{76}As reaction products taken from the literature [65, 66].

Residual nucleus	Half-life [hour]	γ-energy [keV]	Relative γ-intensity per decay [%]
^{71}As	65.28 ± 0.15	174.95 ± 0.04	82.00 ± 0.25
		326.79 ± 0.02	3.03 ± 0.03
		499.87 ± 0.01	3.62 ± 0.02
		1095.49 ± 0.01	4.08 ± 0.06
^{76}As	25.87 ± 0.05	559.10 ± 0.01	45 ± 1
		657.05 ± 0.01	6.2 ± 0.3

taking place in the studied energy range. The cross sections of the (p,α) reactions on Ge isotopes are between 10^{-13} - 10^{-5} barn in the investigated energy region, therefore their γ-radiation was not observable in wide enough energy range.

In summary, it proved feasible to measure the cross sections of the reactions ^{70}Ge(p,γ)^{71}As and ^{76}Ge(p,n)^{76}As in the energy range $E_{c.m.} = 1.6-4.3$ MeV with precision of $\leq$ 12%. Figure 4.2 shows the decay scheme of the ^{71}As and ^{76}As nuclei taken from [65, 66] and in Table 4.2 the decay parameters used for the analysis are summarized.

4.2.2 Target preparation

The targets were made by evaporating natural Ge (purity: 99.99%, impurities typically below ppm) onto thin (2.4 ± 0.7 μm), Al foils with purity of 99.9%. The main impurities of the Al foil are: Iron ($\leq$ 7000 ppm), Silicon ($\leq$ 5000 ppm), Zinc, Copper and Manganese ($\leq$ 1000 ppm). The Al has only one stable isotope, the reaction products of ^{27}Al(p,γ)^{28}Si and ^{27}Al(p,α)^{24}Mg are stable and the (p,n) channel opens only at $E_{c.m.} = 5.59$ MeV which is above our investigated energy range. Furthermore, Al can be easily distinguished from Ge in the Rutherford Backscattering (RBS) spectrum that was used to monitor the target stability during the irradiation (more information about monitoring the target stability can be found in Chapter 6). These reasons make Al as an ideal backing material in low-energy proton-induced reactions using the activation technique. During the evaporation the distance between the backing and the boat was 10 cm. The surface of the target was $f = 1.130$ cm^2. According to this we can assume that the evaporated layer is uniform. Moreover, the diameter of the beam during the irradiation was ≈ 8 mm (see below), this way small unevennesses are integrated out. A layout as well as a picture of the setup used for the evaporation is shown in Fig. 5.2. The thickness of the targets were determined by weighing. The weight of the Al backing was measured before and after the Ge evaporation, from the difference (Δm) the number of the target atom per surface unit (N) could be determined:

$$N = \frac{\frac{\Delta m}{M_{Ge}} \cdot 6.022 \cdot 10^{23}}{f}, \tag{4.1}$$

where $M_{Ge} = 72.64 \pm 0.01$ g is the relative atomic mass of the natural Germanium and f is the area of the target, respectively. In order to verify that the number of target atoms is constant during the irradiation, we repeated the mass measurement of the target also after the irradiation.

The precision of the weight measurement is ± 1 μg and the uncertainty of the isotopic abundance of the ^{71}Ge and ^{76}Ge is 0.17% and 0.07%, respectively [65, 66]. Taking into account these factors and estimating the possible systematic errors, the uncertainty of the number of target atom determination was ± 6%.

The thickness of the targets varied between 50 and 290 μg/cm^2. The proton energy loss was calculated using the SRIM [67] code. Thicker targets were used at low bombarding energies, where the cross section and the corresponding γ-yields are smaller. Even in the case of the thickest target at the lowest proton energy, the energy loss was ≈ 25 keV which is small compared to the 400 keV energy steps (see below).

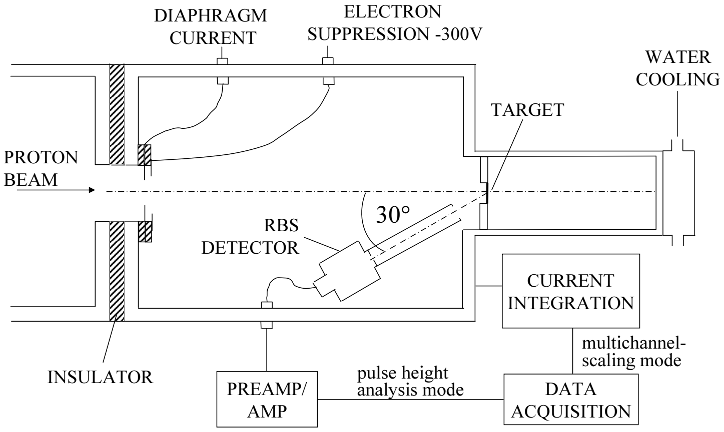

4.3. Figure: Schematic view of the target chamber used for the irradiation.

4.2.3 Irradiations

The irradiations were carried out at the Van de Graaff and cyclotron accelerators of ATOMKI. The energy range ($E_{\mathrm{p}} = 1.6$ to 4.4 MeV) was covered with 400 keV steps since at this mass and energy region no isolated resonances are expected. Several irradiations were repeated with both accelerators and no difference in the measured cross sections were found. A similar chamber to the one designed for the Sr(p,γ) measurements [45] was used, a schematic view of it is shown in Fig. 4.3. The diameter of the beam defining diaphragm is 8 mm — this limits the size of the beamspot. During the experiment defocused beam was used to avoid target deterioration.

The whole chamber was insulated, and served as a Faraday cup. At the entrance of the chamber a diaphragm with −300V secondary electron suppression voltage was used. The number of the incident particles were derived from current measurements. The current integrator was calibrated with precise current sources. Taking into account the uncertainty of the measured current — provided by the current sources — and estimating the

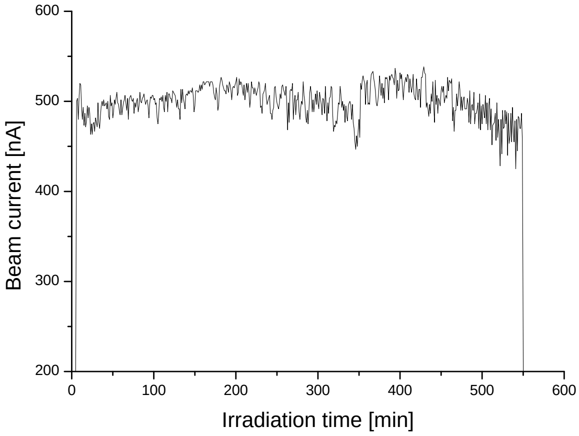

4.4. Figure: Current integrator histogram for the proton irradiation of Ge target at 2.8 MeV. The total collected charge was 1.64 mC.

possible systematic uncertainties, the error in the current measurement was less than 3%.

For calculating the reaction cross section, the proper knowledge of the number of incident particles as a function of time is necessary. The beam current was kept as stable as possible but to follow the changes the current integrator counts were recorded in multichannel scaling mode, stepping the channel in every minute. This recorded current integrator spectrum was then used for the analysis solving the differential equation (see Chapter 4.2.5) of the population and decay of the reaction products numerically. As an example a current integrator spectrum is shown in Fig. 4.4. The collected charge varied between $\approx$ (1.5 - 2) $\times$ 10^{-3} C.

The length of the irradiations varied between 5 and 11 hours depending on the beam energy and the target thickness. At lower energies or if thinner target was used, the irradiations were longer. Before the experiment several beam tests were performed to verify target stability. The results of these target tests showed that there was no deterioration of the targets using a proton beam current less than 500 nA. Moreover, in addition to defocused beam, to avoid target deterioration the backing was watercooled during the

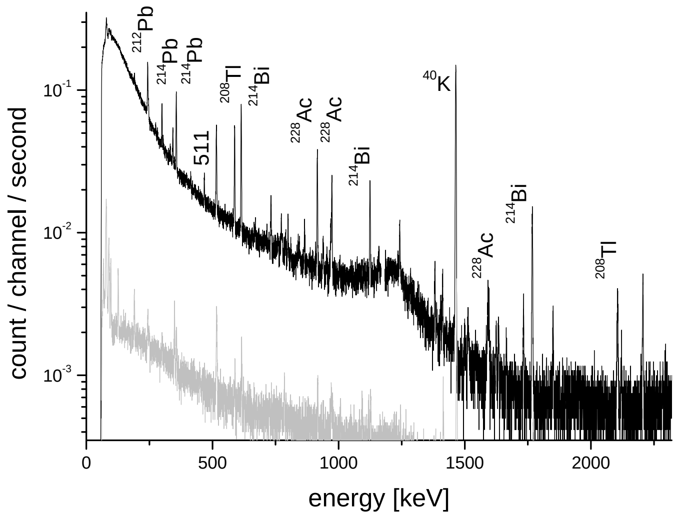

4.5. Figure: γ background measured without lead shielding (black curve) and with lead shield (gray curve). The main background lines are marked.

irradiation. To monitor the target stability, a surface barrier detector was built into the chamber at Θ=150° relative to the beam direction. More details about monitoring the target can be found in Chapter 6.

After the irradiation, the target was removed from the chamber and transported to the γ-counting setup.

4.2.4 Gamma-counting

Between the irradiation and the γ counting, a waiting time of 0.5 h was inserted in order to reduce the yield of the disturbing short-lived activities coming from proton induced reactions on impurities in the target or in the backing. The γ radiation following the β decay of the produced As isotopes was measured with a 40% relative efficiency HPGe detector. The distance between the surface of the detector and the target was 10 cm.

A 5 cm thick lead shield was used to reduce the laboratory background. Figure 4.5 shows laboratory background spectra measured with the HPGe detector used for the γ counting with and without lead shield. As can be seen, the lead shield suppresses the laboratory background with typically a factor of 10 in the case of γ-rays with energy $E_\gamma \leq 1.5$ MeV.

The γ spectra were taken for 10 h and stored regularly in order to follow the decay of the different reaction products. As an example, Fig. 4.6 shows a collected off-line γ spectrum after 4 hours of counting in the case of two different irradiations, normalized to the collected charge. The γ-lines used for the analysis are marked.

The absolute efficiency curve of the detector was measured using calibrated ^{137}Cs, ^{60}Co, and ^{152}Eu sources in the same geometry as for the activity measurements of the irradiated targets. The measured points were fitted with a third-degree logarithmic polynomial to determine the efficiency curve for the energy region of interest. The absolute efficiency curve of the HPGe detector is shown in Fig. 4.7. The efficiency of the detector was also studied with Monte Carlo simulations using the GEANT code [68]. Good agreement between the efficiency curve calculated with GEANT, the polynomial fit and the measured absolute efficiencies was found (see table 4.3). Note, that in table 4.3 only the ^{137}Cs and ^{60}Co measured absolute efficiencies are indicated.

In γ spectroscopy experiments, the so-called summing effect [69] has to be taken into account. The rate of pulses resulting from full absorption of γ-rays with energy of E_γ can be calculated by multiplying the source activity with the emission probability of γ-rays and with the absolute efficiency [69]. However, the yield in the full energy peak can be lower if the reaction product has cascade γ transitions. It may happen that two γ-rays are detected thus leading to a single pulse resulting a count between $E_{\gamma1}$ and $E = E_{\gamma1} + E_{\gamma2}$. This corresponds to an event loss from the $E_{\gamma1}$ full-energy peak. We calculated the probability of event losses for our measuring geometry and found that owing to the relatively large target-detector distance, this effect is well below 0.5% — and this way neglected — in the case of all cascade transitions studied in the present work.

For determining the uncertainty of the detector efficiency the following

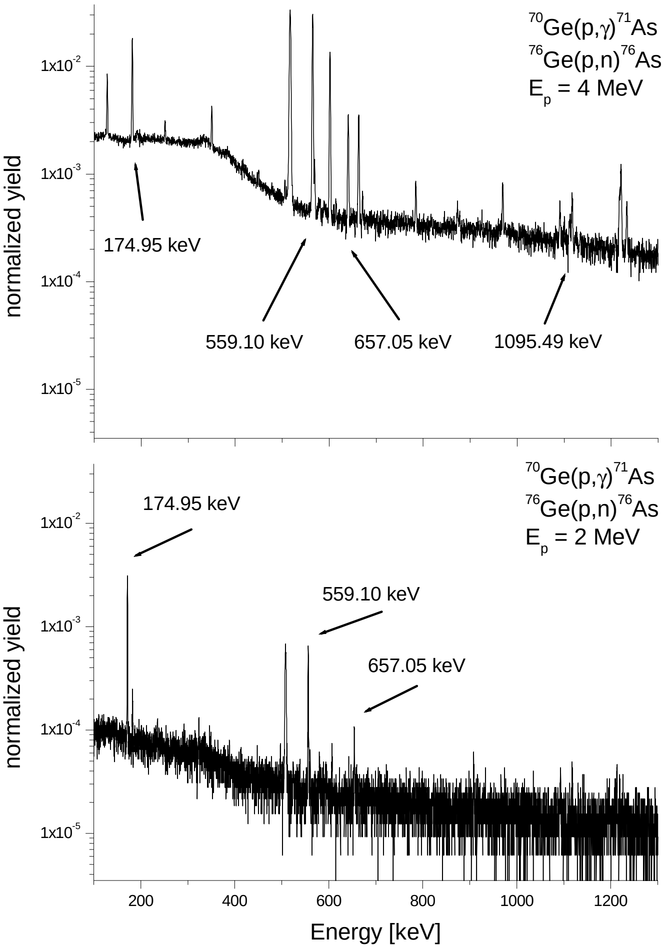

4.6. Figure: Offline γ-spectra taken after the irradiation of natural Germanium targets with 4.0 MeV (upper part) and 2.0 MeV (lower part) proton beam. These spectra were taken in 4 hours and the measured yield is normalized for the collected charge. The peaks used for the analysis are indicated. The other peaks correspond to laboratory background (511 keV), to the decay of ^{74}As (595.85 and 635.78 keV), produced in ^{74}Ge(p,n) and ^{73}Ge(p,γ) reactions and to beam-induced background on impurities in the target or the backing.

4.3. Table: Detector efficiency for the measured γ-lines calculated from the efficiency curve derived using radioactive sources (see below) and determined with GEANT simulations [68].

E_γ $[keV]$	reaction	efficiency (GEANT) x 10^{-3}	efficiency (fit) x 10^{-3}	efficiency (measured) x 10^{-3}
174.95	^{70}Ge(p,γ)^{71}As	11.54	11.82	
326.79	^{70}Ge(p,γ)^{71}As	7.053	7.009	
499.91	^{70}Ge(p,γ)^{71}As	4.748	4.914	
1095.51	^{70}Ge(p,γ)^{71}As	2.626	2.548	
559.10	^{76}Ge(p,n)^{76}As	4.308	4.476	
657.04	^{76}Ge(p,n)^{76}As	3.984	3.910	
514.01	^{85}Rb(p,n)^{85}Sr^{g}	4.823	4.801	
231.64	^{85}Rb(p,n)^{85}Sr^{m}	9.708	9.375	
661.66	^{137}Cs (calibration)	3.810	3.890	3.900
1173.23	^{60}Co (calibration)	2.472	2.407	2.458
1332.50	^{60}Co (calibration)	2.237	2.165	2.193

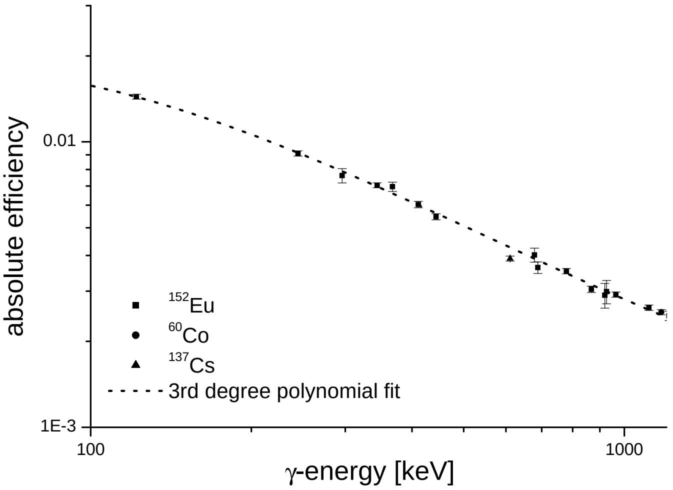

4.7. Figure: Absolute efficiency curve of the HPGe detector used for measuring the γ-activity. For determining the absolute efficiency of the detector calibrated ^{60}Co, ^{137}Cs and ^{152}Eu sources were used. A third degree polynomial fitted to the data is also shown.

factors were taken into account: uncertainty of the level parameters of the different isotopes used for the calibration, the statistical uncertainty of the γ-yields, the uncertainty of the fitting parameters. GEANT calculations had been performed not only to derive the absolute efficiency of the detector, but also to investigate the effect on the efficiency of small variations (3 mm) on the source-detector distance (2.9% change in the absolute efficiency) and small shifts parallel with the detector surface (0.37% change in the absolute efficiency).

Based on these studies the overall uncertainty of the detector efficiency is 6%.

4.2.5 Experimental results

In general the particle capture can lead to the ground or metastable state (if the latter one exists). The number of nuclei in the ground or in the metastable states, G(t) and M(T), respectively can be described with the following equations [42]:

$$\frac{dG(t)}{dt} = -\lambda_g G(t), +\eta\lambda_m M(t) + \sigma_g \Phi(t) N \qquad (4.2)$$

$$\frac{dM(t)}{dt} = -\lambda_m M(t) + \sigma_m \Phi(t) N, \qquad (4.3)$$

where σ_g and σ_m are the cross sections of the reactions leading to the ground and metastable states, respectively, Φ(t) is the proton flux, N describes the number of target atoms per surface unit, η is the branching ratio of the metastable state to the ground state, λ_g and λ_m are the decay constants of the ground and metastable states.

In the case of proton induced reactions on Germanium the equations are more simple because only the ground state of the reaction products of ^{70}Ge(p,γ), ^{76}Ge(p,n) is populated. However, since the (p,n) reaction on ^{85}Rb (see Chapter 5) leads both to the ground and metastable states of ^{85}Sr, both 4.2 and 4.3 equations should be solved.

Analytical solution is possible only if in equation 4.2 and 4.3 the proton beam current is constant. The beam current was kept as stable as possible but there were small variations in the Φ(t) proton flux as it was demonstrated in Fig. 4.4. According to this fact the equations have to be solved numerically. Assuming that the beam current is constant within a small time interval (in our cases Δt = 1 minute was used) we get the following terms for the number of nuclei in the ground and metastable states of the product nucleus after the irradiation, respectively:

$$\begin{aligned}G(t_b) &= \sigma_g N \frac{1-e^{-\lambda_g \Delta t}}{\lambda_g} \sum_{i=1}^{p} \Phi_i e^{-(p-i)\lambda_g \Delta t} + \\ &+ \eta \sigma_m N \left(\frac{1-e^{-\lambda_g \Delta t}}{\lambda_g} - \frac{e^{-\lambda_m \Delta t} - e^{-\lambda_g \Delta t}}{\lambda_g - \lambda_m} \right) \sum_{i=1}^{p} \Phi_i e^{-(p-i)\lambda_g \Delta t} + \\ &+ \sum_{i=1}^{p} \frac{\lambda_m}{\lambda_g - \lambda_m} (e^{-\lambda_m \Delta t} - e^{-\lambda_g \Delta t}) \eta M_{i-1} e^{-(p-i)\lambda_g \Delta t},\end{aligned} \tag{4.4}$$

$$M(t_b) = \sigma_m N \frac{1-e^{-\lambda_m \Delta t}}{\lambda_m} \sum_{i=1}^{p} \Phi_i e^{-(p-i)\lambda_m \Delta t}, \tag{4.5}$$

where t_b is the length of the irradiation and

$$M(i-1) = \sigma_m N \frac{1-e^{-\lambda_m \Delta t}}{\lambda_m} \sum_{k=1}^{i-1} \Phi_i e^{-(i-k)\lambda_m \Delta t}. \tag{4.6}$$

The number of decays from the ground and metastable states during the t_m measuring time after the inserted t_w waiting time are:

$$\begin{aligned}n_g &= G(t_b)(1-e^{-\lambda_g t_m})e^{-\lambda_g t_w} + \frac{\eta \lambda_g \lambda_m M(t_b)}{\lambda_m - \lambda_g} \times \\ &\times \left(\frac{e^{-\lambda_g t_w}}{\lambda_g}(1-e^{-\lambda_g t_m}) - \frac{e^{-\lambda_m t_w}}{\lambda_m}(1-e^{-\lambda_m t_m}) \right),\end{aligned} \tag{4.7}$$

$$n_m = M(t_b)e^{-\lambda_m t_w}(1-e^{-\lambda_m t_m}). \tag{4.8}$$

Using the known parameters, σ_g and σ_m can be determined. Table 4.4 and 4.5 summarize the experimental cross sections and S factors for the two investigated reactions. Figures 4.8 and 4.9 show the results in comparison to the Hauser-Feshbach statistical model predictions, using the NON-SMOKER code [60].

The errors of the center-of-mass energies given in the second column of Table 4.4 and 4.5 correspond to the energy loss in the target calculated with

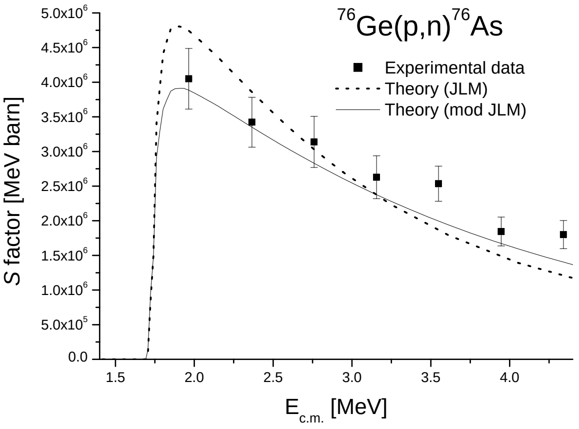

4.8. Figure: Astrophysical S factor as function of proton energy for the reaction ^{76}Ge(p,n)^{76}As compared to NON-SMOKER calculations using the optical potentials of [71, 72] (JLM) and a modified JLM potential with an increased imaginary strength [52] (for more details, see text).

4.4. Table: Experimental cross sections and S factor values of the ^{76}Ge(p,n)^{76}As reaction.

E_{beam} $[keV]$	$E_{c.m.}$ $[keV]$	Cross section $[mbarn]$	S-factor $[10^6 MeV barn]$
2000	1965 ± 13	0.37 ± 0.04	4.0 ± 0.4
2400	2366 ± 4	1.9 ± 0.2	3.4 ± 0.4
2800	2760 ± 9	6.8 ± 0.8	3.1 ± 0.3
3200	3156 ± 10	17 ± 2	2.6 ± 0.3
3600	3549 ± 12	40 ± 4	2.4 ± 0.3
4000	3946 ± 12	62 ± 7	1.8 ± 0.2
4400	4341 ± 13	115 ± 13	1.8 ± 0.2

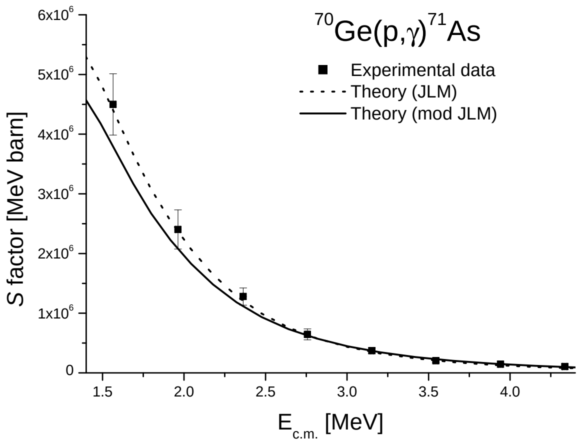

4.9. Figure: Astrophysical S factor as function of proton energy for the reaction ^{70}Ge(p,γ)^{71}As compared to NON-SMOKER calculations using the optical potentials of [71, 72] (JLM) and a modified JLM potential with an increased imaginary strength [52] (for more details, see text).

the SRIM code (5%) and to the energy stability of the beam (± 1 keV in the case of the irradiations done with the Van de Graaf accelerator, 0.5% in the case of the irradiations done with the cyclotron accelerator). The error in the cross section (S factor) values is the quadratic sum of the following partial errors: efficiency of the HPGe detector ($\approx$ 6%), number of target atoms ($\approx$ 6%), current measurement ($\approx$ 3%), uncertainties of the level parameters found in literature [65, 66] ($\leq$ 1%), and counting statistics (0.8 to 11%).

4.3 Discussion and conclusions

The proton capture data are reproduced excellently with the previously published NON-SMOKER Hauser-Feshbach calculation [30, 70]. In the case of the (p,n) data, the reproduction is reasonable although the data indicates a slightly different slope of the S factor as the function of energy.

In order to study the behavior of the calculated S factor, the averaged widths of the proton, neutron and γ channels were systematically and in-

4.5. Table: Experimental cross sections and S factor values of the ^{70}Ge(p,γ)^{71}As reaction.

E_{beam} $[keV]$	$E_{c.m.}$ $[keV]$	Cross section $[mbarn]$	S-factor $[10^6 MeV barn]$
1600	1565 ± 13	0.035 ± 0.004	4.5 ± 0.5
2000	1963 ± 13	0.22 ± 0.03	2.4 ± 0.3
2400	2363 ± 4	0.71 ± 0.08	1.3 ± 0.1
2800	2757 ± 9	1.4 ± 0.2	0.65 ± 0.07
3200	3152 ± 10	2.4 ± 0.3	0.37 ± 0.04
3600	3545 ± 12	3.2 ± 0.4	0.20 ± 0.02
4000	3942 ± 12	4.9 ± 0.6	0.15 ± 0.02
4400	4336 ± 13	6.8 ± 0.8	0.11 ± 0.01

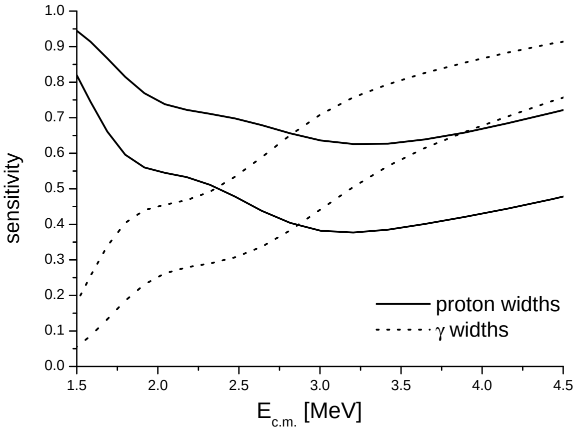

4.10. Figure: Sensitivity of the theoretical ^{70}Ge(p,γ)^{71}As cross section results to variations of the widths as function of proton energy. The area between the solid lines shows the sensitivity to variations of the proton widths (x 2 and x 0.5), the one between the dashed lines is the sensitivity to varied γ widths (x 2 and x 0.5). The sensitivity ranges from 0 (no change) to 1 (the cross section is changed by the same factor as the strength).

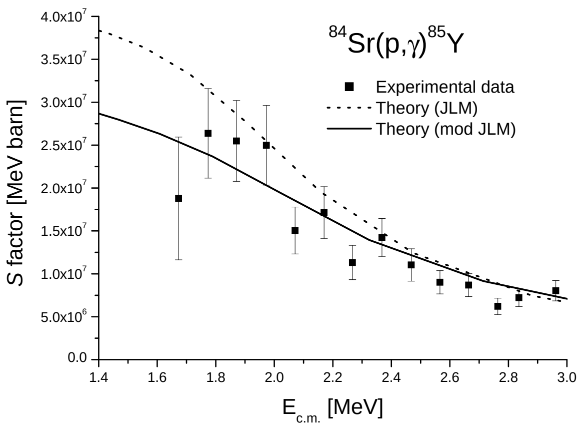

4.11. Figure: Astrophysical S factor as function of proton energy for the reaction ^{84}Sr(p,γ)^{85}Y compared to NON-SMOKER calculations using the optical potentials of [71, 72] (JLM) and a modified JLM potential with an increased imaginary strength [52] (for more details, see text).

dependently varied with a factor of two up and down. The sensitivity (indicated with s) is defined via the variation of the cross section $\Delta\sigma$ = s δ, where δ is the width variation factor chosen between 0.5 and 2.

Not surprisingly the (p,n) channel is sensitive only to the variation of the $\langle\Gamma\rangle_p$ proton width except just above the threshold, where the $\langle\Gamma\rangle_n$ neutron width can also play a role. This indicates, that in the case of the (p,n) reaction it is worth to study the impact of the proton optical potential applied in the calculations for the $\langle\Gamma\rangle_p$ widths.

In the case of the ^{70}Ge(p,γ)^{71}As the situation is more complicated as it is presented in Fig. 4.10. All widths have been varied, however, both the $\langle\Gamma\rangle_p$ proton and $\langle\Gamma\rangle_\gamma$ γ widths have been found important. As it is demonstrated in Fig. 4.10 below about 2.5 MeV the S factor is mostly sensitive for changing the $\langle\Gamma\rangle_p$ proton widths and above this energy the sensitivity for $\langle\Gamma\rangle_\gamma$ γ widths becomes comparable or larger. The agreement between the theory and the experimental data demonstrates that the $\langle\Gamma\rangle_p$ proton width at low energies and the $\langle\Gamma\rangle_\gamma$ γ widths at the upper half of the investigated energy region are described well.

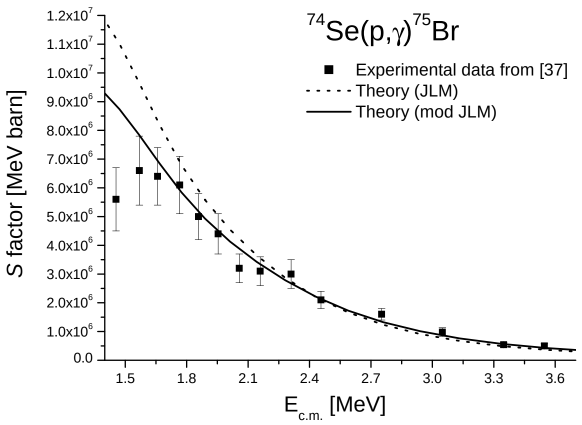

4.12. Figure: Astrophysical S factor as function of proton energy for the reaction ^{74}Se(p,γ)^{75}Br compared to NON-SMOKER calculations using the optical potentials of [71, 72] (JLM) and a modified JLM potential with an increased imaginary strength [52] (for more details, see text).

4.6. Table: Astrophysical reaction rates of the reaction ^{70}Ge(p,γ)^{71}As calculated from the experimental data.

Temperature [10^9 K]	Reaction Rate [cm^{3}s^{-1}mole^{-1}]
2.50	$(4.474\pm0.584)\times10^2$
2.75	$(9.660\pm1.282)\times10^2$
3.00	$(1.862\pm0.250)\times10^3$
3.25	$(3.284\pm0.445)\times10^3$
3.50	$(5.393\pm0.737)\times10^3$
3.75	$(8.357\pm1.148)\times10^3$
4.00	$(1.234\pm0.170)\times10^4$
4.25	$(1.749\pm0.242)\times10^4$
4.50	$(2.394\pm0.333)\times10^4$
4.75	$(3.180\pm0.444)\times10^4$
5.00	$(4.116\pm0.576)\times10^4$

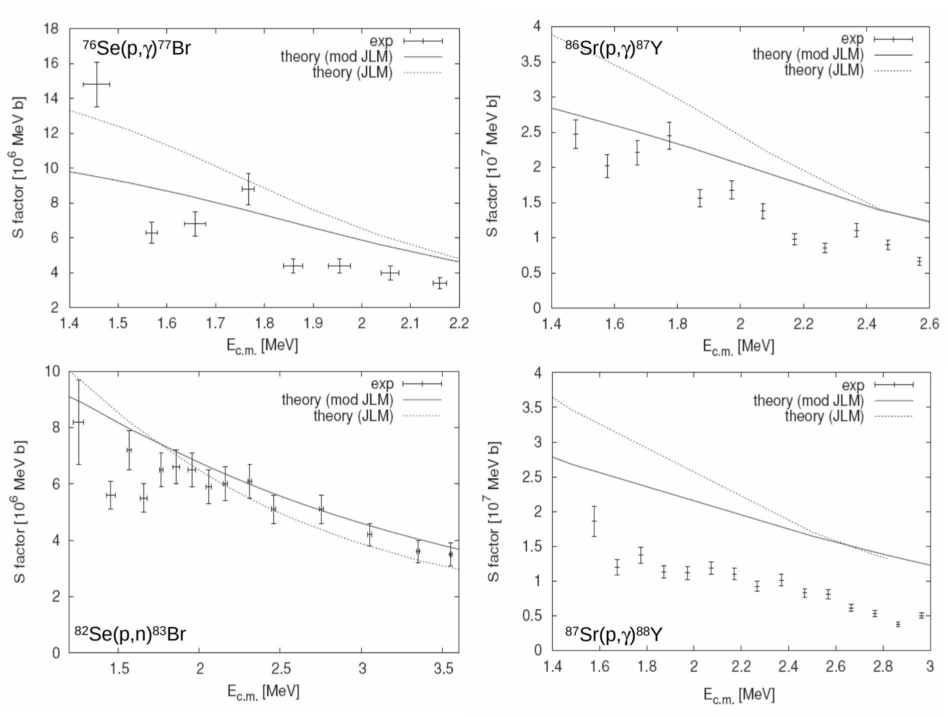

4.13. Figure: Astrophysical *S* factor as function of proton energy for the reaction ^{76}Se(p,γ)^{77}Br, ^{82}Se(p,n)^{82}Br, ^{86}Sr(p,γ)^{87}Y and ^{87}Sr(p,γ)^{88}Y compared to NON-SMOKER calculations using the optical potentials of [71, 72] (JLM) and a modified JLM potential with an increased imaginary strength [52] (for more details, see text).

The proton optical potential used for the above discussed studies is the widely-used semimicroscopic potential [71] with low energy modifications [72] (It is addressed in the future as JLM potential). We have attempted to improve the JLM potential by modifying the strength of the imaginary part (modified JLM). It was found that the best compromise for describing both the (p,γ) and (p,n) data is the increase of the imaginary strength with approximately 70% and keeping the real part constant. It can be seen clearly on Fig. 4.8 and 4.9 how the modification improves the results of the calculated S factors. Proton-induced reactions in this mass range were already studied on Se and Sr isotopes by Gyürky *et al.*, [45, 49] and as a demonstration of the reliability of the new, modified potential used as input for the calculations the improved predictions for the ^{84}Sr(p,γ)^{85}Y and ^{74}Se(p,γ)^{75}Br reactions in Fig. 4.11 and 4.12 are shown. Further comparison between the existing experimental data in this mass and energy range and the theoretical calculations can be seen in Fig 4.13. In summary, a statistical model calculation using this improved potential can give a better description for the measured cross sections in this mass and energy range. However, it is yet an open question, whether the modification is also applicable to other mass ranges (see Chapter 5 and 6).

In the last part of the theoretical investigations the astrophysical reaction rates for the investigated reactions will be provided. As it was discussed, the relevant temperatures of the investigated reactions are around 2-3 GK [20, 27]. The reaction rates are directly calculated from the experimental S factors by linear interpolation using the EXP2RATE code [73]. Table 4.6 contains the ground state reaction rates for the ^{70}Ge(p,γ)^{71}As for T = (2.5 - 5) x 10^9 K. Due to the (p,n) threshold the reaction rate of ^{76}Ge(p,n)^{76}As can be calculated in a broader temperature range between T = (0.25 - 4) x 10^9 K and it is given in Table 4.7.

It has to be noted that the reaction rate of both the ^{70}Ge(p,γ)^{71}As and the ^{76}Ge(p,n)^{76}As has been derived by Rougthon *et al.*, [74] from thick target yields. Usually the reaction rate is derived from the measured cross

4.7. Table: Astrophysical reaction rates of the reaction ^{76}Ge(p,n)^{76}As calculated from the experimental data.

Temperature [10^9 K]	Reaction Rate [$\mathrm{cm^3 s^{-1} mole^{-1}}$]
0.50	$(3.086 \pm 0.012) \times 10^{-12}$
0.75	$(2.118 \pm 0.040) \times 10^{-6}$
1.00	$(1.912 \pm 0.071) \times 10^{-3}$
1.25	$(1.222 \pm 0.066) \times 10^{-1}$
1.50	$(2.088 \pm 0.142) \times 10^{0}$
1.75	$(1.683 \pm 0.133) \times 10^{1}$
2.00	$(8.487 \pm 0.746) \times 10^{1}$
2.25	$(3.128 \pm 0.296) \times 10^{2}$
2.50	$(9.231 \pm 0.919) \times 10^{2}$
2.75	$(2.310 \pm 0.239) \times 10^{3}$
3.00	$(5.091 \pm 0.542) \times 10^{3}$
3.25	$(1.013 \pm 0.110) \times 10^{4}$
3.50	$(1.856 \pm 0.205) \times 10^{4}$
3.75	$(3.173 \pm 0.355) \times 10^{4}$
4.00	$(5.114 \pm 0.580) \times 10^{4}$

sections (see Chapter 2). However, it was shown that it is possible to compute $\langle \sigma v \rangle$ directly from thick target yields [74] and the calculations in the work of Rougthon *et al.*, was based on this method. However, it should be emphasized that this method involves extrapolation both above and below the measured energies [74]. It was found that the rates of Rougthon *et al.*, are lower than ours by about 35% and 20% in the case of ^{70}Ge(p,γ)^{71}As and ^{76}Ge(p,n)^{76}As reaction, respectively.

4.4 Summary

The cross section of ^{70}Ge(p,γ)^{71}As and ^{76}Ge(p,n)^{76}As reactions was measured within the astrophysically relevant energy region using the activation technique. The results were compared to statistical model calculation performed with the NON-SMOKER code using standard input parameters.

Since a difference between the measured and the calculated S factors was found, a sensitivity study has been carried out to investigate the behavior of the statistical model calculation when varying the nuclear inputs like proton, neutron and γ widths. It was found that the cross sections depend sensitively on the proton widths computed from the proton-nucleus optical potential.

To give a better description of the experimental data, we suggested modifying the imaginary part of the potential with an increased strength of 70%. The cross sections of the previous as well as the present (p,γ) and (p,n) reactions were compared to the statistical model calculations using the modified potential as input and a better agreement between the experimental data and the theoretical calculations was found.

5 Chapter

The cross section measurement of the ^{85}Rb(p,n)^{85}Sr reaction

5.1 Introduction

The reliability of the p process model calculations are determined by the precision of nuclear input parameters like α, proton, neutron and γ widths, level densities, etc. It was proved recently [52] (see Chapter 4) that (p,n) reactions can provide important supplementary information on the optical potential used to calculate the interaction between protons and target nuclei. In low-energy (p,γ) reactions, cross sections can be sensitive to the proton as well as the γ strength. Conversely, in (p,n) reactions the sensitivity is highest to a variation in the proton width because the neutron width is much larger, thus suppressing the sensitivity to the width in the other channel.

Compared to the well-studied (p,γ) reactions [41-53] there is only limited experimental information available on low-energy (p,n) cross sections in the mass region of light p nuclei [63]. This fact alone necessitates to extend the nuclear database relevant to the astrophysical p process.

Additionally, it was found in systematic p process simulations that not only photodisintegration reactions are important but also (p,n) reactions — particularly the ^{85}Rb(p,n)^{85}Sr reaction — can strongly influence the final p

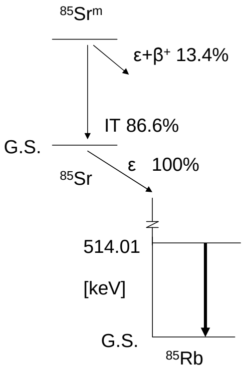

5.1. Figure: Decay scheme of ^{85,85m}Sr [75, 76]. The γ transition used for the analysis are indicated.

abundances [28]. As it is shown in the following, the astrophysical rate can directly be derived from the (p,n) data for this reaction, despite the target being in the ground state and the negative reaction Q value.

In Chapter 4 a modified proton optical potential has been introduced for getting a better description of the measured proton induced reactions. A further test for this potential can be done with measuring the cross section of the ^{85}Rb(p,n)^{85}Sr reaction and compare the data with the theoretical cross section calculations.

5.2 The ^{85}Rb(p,n)^{85}Sr reaction

Similarly to the discussion of proton-induced cross section measurement on Germanium isotopes, first the details of the experiment will be described. In Chapter 5.2.4 the experimental results are discussed and the reaction rate calculation necessary for astrophysical application is provided.

5.2.1 Feature of the investigated reaction

The (p,n) reaction on ^{85}Rb leads to the ground (^{85}Sr^{g}) and isomeric states (^{85}Sr^{m}) of ^{85}Sr isotope. The ^{85}Sr^{g} decays by electron capture to ^{85}Rb and

5.1. Table: Decay parameters of ^{85}Rb(p,n)^{85}Sr^{g,m} reaction products [75].

Residual nucleus	Half-life	Gamma energy [keV]	Relative γ-intensity per decay [%]
^{85}Sr^{g}	64.84 ± 0.02 day	514.01 ± 0.02	96 ± 4
^{85}Sr^{m}	67.63 ± 0.04 min	231.86 ± 0.01	84.4 ± 0.2

the ^{85}Sr^{m} with internal transition to the ground state of ^{85}Sr (86.6 ± 4%) as well as with electron capture and β^{+} to ^{85}Rb (13.4 ± 4%) [75, 76]. For determining the cross section of the ^{85}Rb(p,n)^{85}Sr^{g} the 514 keV gamma line and for measuring the cross section of the ^{85}Rb(p,n)^{85}Sr^{m} the 231 keV gamma line was used. The decay parameters of ^{85}Sr^{g,m} isotopes are summarized in Table 5.1 and the decay scheme is shown in Fig. 5.1

The main experimental challenge was to separate the transition of E_{γ} = 514 keV from the usually broad annihilation peak coming from beam-induced reactions on impurities of the target and the backing. The contribution from the laboratory background to the yield of the 511 keV peak was negligible as it was demonstrated in the repeated activity measurement (see lower part of Fig. 5.6). It is only possible to separate the investigated 514 keV peak from the annihilation peak if its yield is higher or the yields are comparable. In the following it is described how this requirement was fulfilled.

5.2.2 Target preparation and target-thickness determination

The element Rubidium is an alkali metal. The alkali metals are highly reactive metals, igniting in air and reacting violently with water or oxidants. Therefore, the targets have to be produced from their compounds. The most important aspect for choosing RbCl as target material was that there is no disturbing activity coming from proton induced reactions on Chlorine isotopes since the products are stable or short lived isotopes. In Table 5.2 the reaction products of proton-induced reactions on RbCl are listed.

The targets were made with evaporating chemically pure (99.99%) nat-

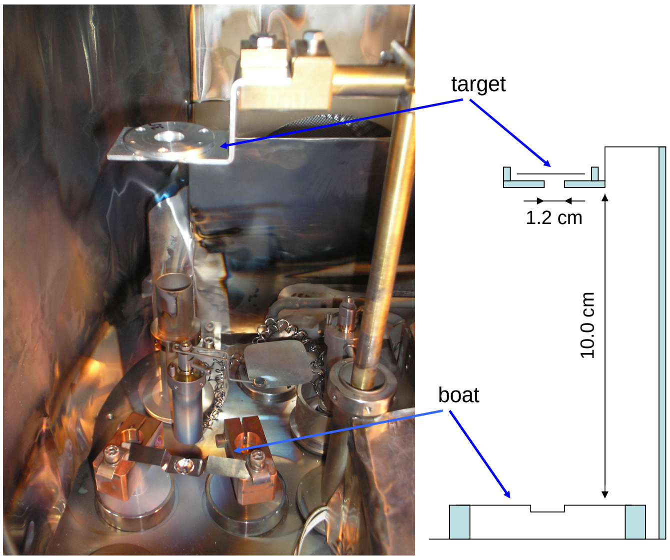

5.2. Figure: Picture and schematic view of the evaporator used for producing the RbCl and Germanium targets.

ural RbCl onto two different kinds of thin Aluminium foils. The thicker one had a chemical purity of 99.999% and thickness of 50 μm, the purity and the thickness of the thinner one was 99% and 2.4 μm, respectively.

During the evaporation the distance between the backing and the Tantalum boat was 10 cm. Tantalum is ideal material for using as crucible since its melting point is above 3000 K. Figure 5.2 shows a picture and a schematic view of setup used for evaporating RbCl.

The thickness of the targets were different, thicker ones (on thicker backings) were used at lower and thinner ones (on thinner backing) at higher energies. Owing to this selection, the yield of the two peaks (the investigated 514 keV transition and the 511 keV annihilation peak) was comparable as it is demonstrated in the upper part of Fig. 5.6.

Two different methods for determining the number of target atoms were used. In the case of the targets evaporated onto the thinner backing weighing was used i.e. we measured the weight of the foil before and after the

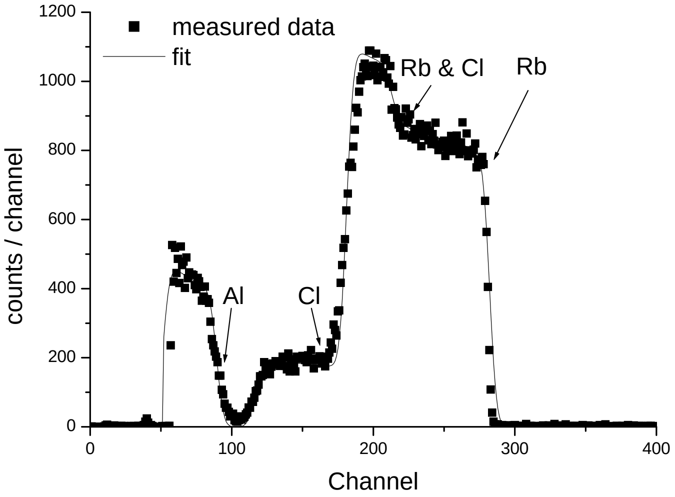

5.3. Figure: Typical RBS spectra measured with 2 MeV He$^+$ beam. The uncertainty of the points is within the size of the symbols. The fit to the measured data is also shown.

evaporation and from the difference — assuming that our target is uniform — it is possible to calculate the number of target atoms (for details see Chapter 4).

Because of the weight of the thicker backing it was not possible to use the above discussed procedure, the absolute number of target atoms and the uniformity of the layers were determined before and after the irradiation by Rutherford Backscattering method (RBS) using the Scanning Nuclear Microprobe facility of ATOMKI [76-79]. A schematic view and a picture of the chamber used for the target thickness determination is shown in Fig. 5.4. A 2 MeV He$^+$ beam provided by the Van de Graaff accelerator of ATOMKI was focused down to 3x3 μm^2 and was scanned over a 75x75 μm^2 area of the target. To measure the yield of the backscattered α-particles two Ion-Implanted Si detectors of 18 keV system resolution and 50 mm^2 area were applied at $\Theta = 165°$ ($\Omega = 32.5$ msrad) and $\Theta = 135$ ° ($\Omega = 57.3$ msrad) simultaneously. The total deposited charge was between 80 and 130 nC. The RBS spectra were evaluated with the RBX computer code [81]. Figure

5.2. Table: Proton-induced reactions on Rubidium and Chlorine isotopes

target nucleus	reaction	product nucleus	limitation
^{85}Rb	(p,γ)	^{86}Sr	reaction product is stable
^{85}Rb	(p,n)	^{85}Sr^{g}	no
	(p,n)	^{85}Sr^{m}	no
^{85}Rb	(p,α)	^{82}Kr	reaction product is stable
^{87}Rb	(p,γ)	^{88}Sr	reaction product is stable
^{87}Rb	(p,n)	^{87}Sr^{g}	reaction product is stable
	(p,n)	^{87}Sr^{m}	not useful without ground state σ(E)
^{87}Rb	(p,α)	^{84}Kr	reaction product is stable
^{35}Cl	(p,γ)	^{36}Ar	reaction product is stable
^{35}Cl	(p,n)	^{35}Ar	$T_{1/2} = 1.78$ s
^{35}Cl	(p,α)	^{32}S	reaction product is stable
^{37}Cl	(p,γ)	^{38}Ar	reaction product is stable
^{37}Cl	(p,n)	^{37}Ar	no γ emission
^{37}Cl	(p,α)	^{34}S	reaction product is stable

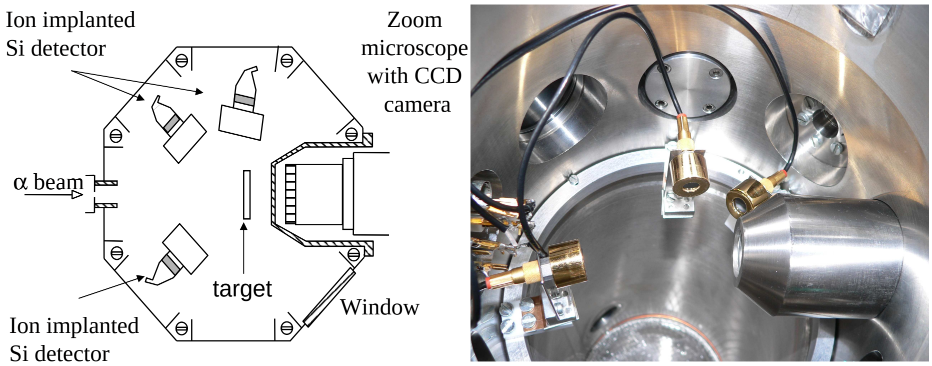

5.4. Figure: Schematic view and a picture of the chamber used for measuring the number of target atoms via the RBS method (see text).

5.3 shows a typical measured RBS spectrum. The thickness of the targets were between 60 and 250 μg/cm^2. The precision of the determination of the number of target atoms was better than 3%. We found that the layers were uniform, the thickness distribution was flat within 1%. Using this method it was also possible to monitor the ratio of the Rb to Cl. It was found that the chemical composition was not affected by the evaporation and the irradiation, it remains 50 : 50 (± 1%). To inspect the weight measurement in the case of targets on the thinner backings the absolute number of target atoms were derived also with RBS method and perfect agreement — within 2% — was found.

5.2.3 Irradiation

The thin RbCl targets were bombarded with a proton beam of 600 nA typical intensity, provided by the Van de Graaff and cyclotron accelerators of ATOMKI. Figure 5.5 shows the beam intensity as a function of time for two different irradiations. In the second case, the beam provided by the cyclotron was not stable, for this reason the irradiation was repeated. The energy range of the proton beam between 2 and 4 MeV was covered with 200 keV steps since we wanted to investigate sensitively the region

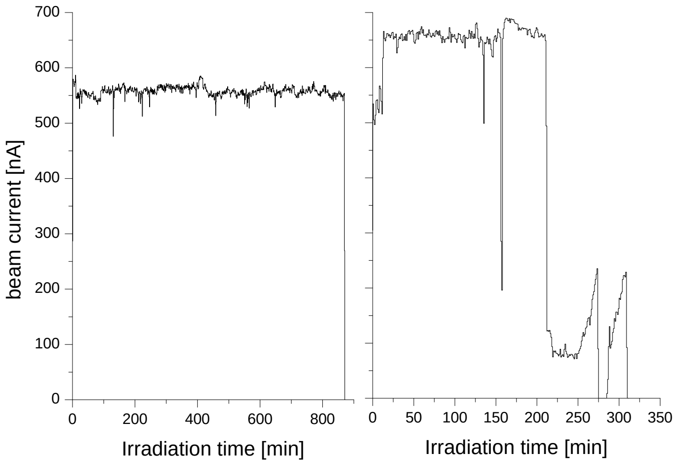

5.5. Figure: Current Integrator histogram in the case of two different irradiations at E$_p$ = 2.4 MeV (Van de Graaff accelerator) and E$_p$ = 3.6 MeV (cyclotron accelerator). In the case of the irradiation shown in right panel (cyclotron), the ion source was not stable, for this reason the irradiation was repeated.

where the theoretical predictions of the JLM [71, 72] and the modified JLM proton optical potential differs (for detailed information of these potentials see Chapter 4). The low energy irradiations (2.0, 2.4 and 2.6 MeV) have been carried out using the Van de Graaff. At and above 2.6 MeV the cyclotron accelerator was used. The cross section at E$_p$ = 2.6 MeV was measured with both accelerators and no difference was found. Each irradiation lasted approximately 8 hours.

5.2.4 Gamma-counting and results

For measuring the induced γ-activity the same lead shielded HPGe detector was used as for investigating the proton-induced reactions on Germanium isotopes (see Chapter 4). The distance between the surface of the detector and the target was 10 cm — at this distance the detector efficiency is well known (see Chapter 4.2.4 for more details)— this way the γ-yield was reasonable and the summing effect was negligible. After each irradiation 1 hour

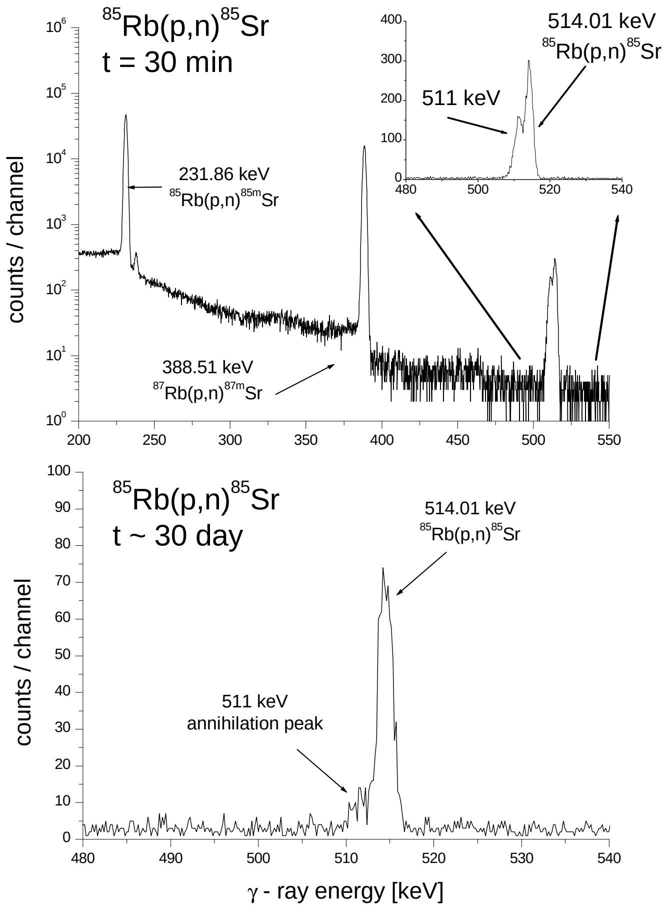

5.6. Figure: Off-line γ spectrum taken 30 m after the irradiation at 3.8 MeV (upper panel). The 514 keV peak from the ^{85}Rb(p,n)^{85}Sr reaction is well separated from the annihilation peak. The lower panel shows a typical spectrum taken in the repeated activity measurement approximately one month after the irradiation of the target with 2.6 MeV protons. The acquisition time was 30 minutes in both cases.

waiting time was applied to let the short lived disturbing activities disappear. The γ spectra were taken for 12 hours. Since the half-life of the ^{85}Sr^{g} is relatively long 64.84 days, the activity was remeasured in the case of each target approximately 1 month later. Fig. 5.6 shows two typical measured spectra, the upper spectrum was taken just after the irradiation, while the lower spectrum approximately one month later. Except for the 388.53 keV γ-line from the ^{87}Rb(p,n)^{87}Rb^{m} reaction no disturbing γ-transitions were observed.

Based on the activity measurement one hour after the irradiation and the repeated activity measurement one month later, two separated analysis were done in the case of the ^{85}Rb(p,n)^{85}Sr^{g} reaction. The derived cross sections agree within 4%. The final results were calculated from the average weighted by the statistical uncertainty of the two independent γ counting. The half life of ^{85}Sr^{m} is about 1 hour, therefore in that case it was not possible to repeat the activity measurement.

The measured total cross sections cover 3 orders of magnitude, ranging from 0.058 to 19.65 mb. Table 5.3 lists the resulted cross sections and S factors. The uncertainty of the cross section values is the quadratic sum of the following partial errors: efficiency of the HPGe detector (6%), number of target atoms (3%), current measurement (3%), counting statistics (0.2-4%) and decay parameters ($\leq$ 4%). The errors of the center-of-mass energies given in Table 5.3 correspond to the energy loss in the target calculated with the SRIM code (5%) and for the energy stability of the beam (± 1 keV in the case of the irradiations with the Van de Graaff accelerator, 0.5% in the case of the irradiations with the cyclotron accelerator).

The cross section of the ^{85}Rb(p,n)^{85}Sr reaction was already measured by Kastleiner *et al.*, [82] at several proton energies between $E_{c.m.} = 3.1$ and 70.6 MeV for medical application. Unfortunately, the accuracy of the low energy points are not sufficient for astrophysical applications mainly because of the large uncertainty in the c.m. energies — typically 0.3-0.5 MeV. Moreover, there is only one point in the astrophysical relevant energy region with ± 0.5

5.3. Table: Experimental cross section and S factor values of the ^{85}Rb(p,n)^{85}Sr reaction.

$E_{c.m.}$ $[keV]$	Ground state cross section $[mbarn]$	Isomeric state cross section $[mbarn]$	Total cross section $[mbarn]$	S-factor $[10^6 MeV barn]$
2158 ± 8	0.050 ± 0.005	0.008 ± 0.001	0.058 ± 0.006	7.13 ± 0.67
2341 ± 16	0.185 ± 0.013	0.039 ± 0.006	0.224 ± 0.019	11.22 ± 0.96
2552 ± 27	0.422 ± 0.03	0.147 ± 0.022	0.569 ± 0.051	11.35 ± 1.02
2566 ± 26	0.420 ± 0.03	0.162 ± 0.023	0.582 ± 0.057	11.01 ± 1.04
2765 ± 28	0.920 ± 0.09	0.282 ± 0.031	1.202 ± 0.118	10.65 ± 1.05
2963 ± 30	1.734 ± 0.17	0.391 ± 0.039	2.125 ± 0.234	9.59 ± 0.92
3156 ± 32	3.155 ± 0.3	0.612 ± 0.06	3.767 ± 0.38	9.40 ± 0.87
3342 ± 35	4.547 ± 0.4	1.107 ± 0.14	5.654 ± 0.53	8.37 ± 0.79
3551 ± 36	7.672 ± 0.6	1.931 ± 0.23	9.603 ± 0.87	8.32 ± 0.76
3754 ± 38	11.62 ± 0.9	2.694 ± 0.32	14.32 ± 1.31	7.73 ± 0.66
3952 ± 40	14.42 ± 1.2	5.227 ± 0.64	19.65 ± 1.82	6.93 ± 0.64

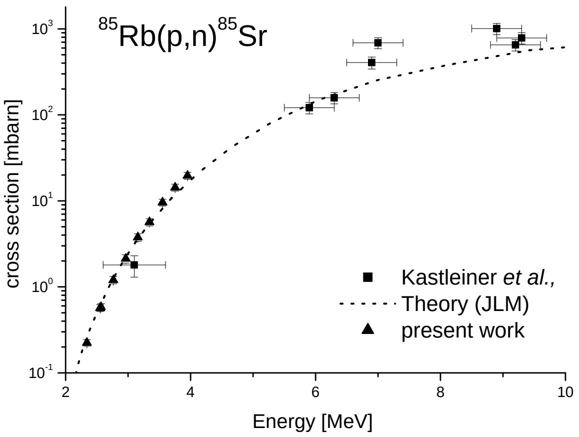

5.7. Figure: Cross section of the ^{85}Rb(p,n)^{85}Sr^{g,m} reaction. The dasched curve corresponds to statistical model calculations with the standard JLM potential [71, 72] performed with the NON-SMOKER code [60]. The triangles are corresponding to the results of the present work. Please note that this case the uncertainty is below the size of the dots this case.

MeV uncertainty in $E_{c.m.}$ and 33% uncertainty in the cross section. Figure 5.7 shows the experimental results of [82], the cross sections derived in the present work and the results of the statistical model calculations performed with the NON-SMOKER code (please note the logaritmic scale).

The measured astrophysical S factors (obtained from the total cross sections leading to the isomeric and ground state of ^{85}Sr) are compared to theoretical predictions obtained with the NON-SMOKER code [60, 30] in Fig. 5.8. Two different proton optical potentials were used as input for the calculations: the well know JLM potential and the modified JLM potential (for details see Chapter 4). As can be seen in Fig. 5.8, the theoretical energy dependence of the resulting S factor is slightly steeper than the data in the case of the JLM potential [71], although there is a general agreement in magnitude. In the energy range covered by the measurement, the proton width is smaller than the neutron width (except close to the threshold) and thus uncertainties in the description of the proton width (and proton

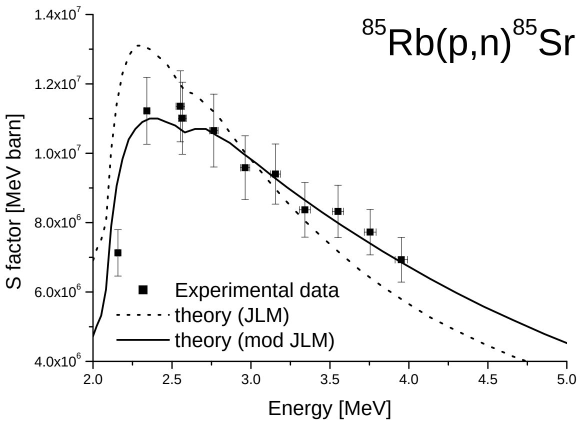

5.8. Figure: Astrophysical S factor of the ^{85}Rb(p,n)^{85}Sr reaction. The lines correspond to Hauser-Feshbach statistical model calculations performed with the NON-SMOKER code [60] using the optical potential of [71, 72] (JLM) and a modified JLM potential with increased imaginary strength [52].

transmission coefficient) will fully impact the resulting S factor. Figure 5.8 shows also the prediction resulting from the use of the JLM potential with the imaginary strength increased by 70%. This modification was introduced in Chapter 4, leading to an improvement of the reproduction of (p,γ) as well as (p,n) data. Here, we find that the energy dependence of the theoretical S factor is changed by the modification on a way showing perfect agreement with the new data.

5.3 Conclusions

As it was discussed previously, the astrophysical reaction rate to be used in reaction network calculations cannot be measured directly. Contrary to the astrophysical plasma, where the excited states are thermally populated, in laboratory only reactions on the ground state of the target can be investigated. A measure of the influence of the excited target states is given by the so-called stellar enhancement factor:

5.4. Table: Stellar enhancement factors for the investigated reactions in the relevant temperature region [83]. The Q value of the reactions are also indicated.

reaction	Q value [MeV]	temperature [GK]	stellar enhancement factor
^{70}Ge(p,γ)^{71}As	4.62	2.0 - 4.0	0.99 - 1.00
^{76}Ge(p,n)^{76}As	-1.71	2.0 - 4.0	1.08 - 1.02
^{85}Rb(p,n)^{85}Sr	-1.85	2.5 - 3.5	1.08 - 1.03
^{85}Sr(n,p)^{85}Rb	1.85	2.5 - 3.5	2.62 - 3.86
^{106}Cd(p,γ)^{107}In	3.72	2.5 - 4.0	1.01 - 1.05
^{108}Cd(p,γ)^{109}In	4.52	2.5 - 4.0	1.00 - 1.01

$$f = \langle\sigma v\rangle_{stellar} / \langle\sigma v\rangle_{g.s.}. \tag{5.1}$$

The factor f is usually much larger for the reverse reaction B(b,a)A (defined by having negative Q value) than for the forward reaction A(a,b)B (being the one with positive Q value) because more excited states can be populated in nucleus B than in nucleus A. Therefore, more astrophysically relevant transitions are neglected when a reaction with negative Q value studied experimentally. Furthermore, rates employed in reaction networks often use fitted rates for the forward and backward reaction which are derived from the same rate for one direction to ensure compatibility and numerical stability. For that reason, the fit for the reverse stellar rate is derived from the one for the forward rate by applying detailed balance. This is the preferred approach because the relation between backward and forward rate,

$$\langle\sigma v\rangle^{\mathrm{B(b,a)A}}_{\mathrm{stellar}} \propto e^{-\frac{Q_{\mathrm{A(a,b)B}}}{kT}} \langle\sigma v\rangle^{\mathrm{A(a,b)B}}_{\mathrm{stellar}}, \tag{5.2}$$

includes the exponential which would enhance fit inaccuracies when starting from the reverse rate with $Q < 0$ (see also [30]).

For the above reasons, one can would conclude that a measurement of a (p,n) reaction on a proton-rich target is not suited to derive stellar rates for use in astrophysical reaction networks. However, the situation is different for the reaction ^{85}Rb(p,n)^{85}Sr. A comparison of $f_{\mathrm{pn}} = 1.08 - 1.03$ and $f_{\mathrm{np}} = 2.62 - 3.86$ (see Table 5.4) shows that the transitions to excited states of ^{85}Sr are more important than those to states in ^{85}Rb in the relevant plasma temperature range of $2 \leq T \leq 4$ GK. The large f_{np} is due to the spin structure of the available nuclear levels and especially the large ground state spin of ^{85}Sr ($J^{\pi} = 9/2^{+}$). Because of its large spin, it is connected to the (dominating) low spin states in ^{85}Rb through higher partial waves. The transitions from the ground state are suppressed by the centrifugal barrier relative to transitions from excited states and the latter will quickly become important, even at low temperature.

More important for our measurement is the almost negligible stellar enhancement f_{pn}. This is due to the small $|Q| = 1.847$ MeV. The proton transmission coefficients to and from the excited states of ^{85}Rb are suppressed for small relative proton energies because of the Coulomb barrier and there are only a few transition with larger proton energies due to the small difference in binding energy of ^{85}Rb and the compound nucleus. As shown by the small f_{pn}, the transition from the ground state of ^{85}Rb dominates the proton channel.

Obviously, a Coulomb suppression is not present in the neutron channel. Therefore, it is better to measure the (p,n) direction in this case. Thus, the important transitions to the states in ^{85}Sr are included in our data and the small impact of transitions from excited states in ^{85}Rb is within the experimental error. By computing the forward rates directly from the backward rates the complication with the negative Q value in fitted data is also avoided. Table 5.4 summarizes the Q values and the stellar enhancement factors for all reactions investigated in the present work.

Table 5.5 gives the stellar rates for ^{85}Rb(p,n)^{85}Sr as well as for ^{85}Sr(n,p)^{85}Rb reactions. Our data covers an energy range sufficient to compute the rates up to 4 GK. Because of the excellent agreement between theory and experiment, we supplement the data with the theoretical values

5.5. Table: Astrophysical reaction rates of the reactions ^{85}Rb(p,n)^{85}Sr and ^{85}Sr(n,p)^{85}Rb computed from the experimental data. The values in italics are at temperatures where the experimental data mostly contribute to the rate. The other values are computed by supplementing theoretical cross sections using the modified optical potential.

Temperature [10^9 K]	^{85}Rb(p,n)^{85}Sr [cm^{3}s^{-1}mole^{-1}]	^{85}Sr(n,p)^{85}Rb [cm^{3}s^{-1}mole^{-1}]
0.10	$(1.72\pm0.17)\times10^{-89}$	$(1.19\pm0.2)\times10^{4}$
0.20	$(8.33\pm0.83)\times10^{-43}$	$(1.74\pm0.17)\times10^{4}$
0.40	$(2.26\pm0.23)\times10^{-19}$	$(2.55\pm0.26)\times10^{4}$
0.60	$(1.74\pm0.17)\times10^{-11}$	$(3.49\pm0.35)\times10^{4}$
0.80	$(1.77\pm0.18)\times10^{-7}$	$(4.80\pm0.48)\times10^{4}$
1.00	$(5.07\pm0.51)\times10^{-5}$	$(6.57\pm0.66)\times10^{4}$
1.50	$(1.28\pm0.13)\times10^{-1}$	$(1.35\pm0.14)\times10^{5}$
2.00	*(8.30 ± 0.83)*	*$(2.56\pm0.26)\times10^{5}$*
2.50	*$(1.21\pm0.12)\times10^{2}$*	*$(4.57\pm0.46)\times10^{5}$*
3.00	*$(8.22\pm0.82)\times10^{2}$*	*$(7.81\pm0.78)\times10^{5}$*
3.50	*$(3.56\pm0.36)\times10^{3}$*	*$(1.28\pm0.13)\times10^{6}$*
4.00	*$(1.15\pm0.12)\times10^{4}$*	*$(2.04\pm0.20)\times10^{6}$*
4.50	$(3.03\pm0.30)\times10^{4}$	$(3.17\pm0.32)\times10^{6}$
5.00	$(6.89\pm0.69)\times10^{4}$	$(4.76\pm0.48)\times10^{6}$
6.00	$(2.60\pm0.26)\times10^{5}$	$(9.52\pm0.95)\times10^{6}$
7.00	$(7.14\pm0.71)\times10^{5}$	$(1.54\pm0.15)\times10^{7}$
8.00	$(1.50\pm0.15)\times10^{6}$	$(2.01\pm0.20)\times10^{7}$
9.00	$(2.50\pm0.25)\times10^{6}$	$(2.18\pm0.22)\times10^{7}$
10.00	$(3.44\pm0.34)\times10^{6}$	$(2.05\pm0.21)\times10^{7}$

to compute the rates at higher temperatures.

5.4 Summary

The cross section of the ^{85}Rb(p,n)^{85}Sr^{g,m} reaction was measured with high precision in the astrophysically relevant energy region for the *p* process in order to provide an independent test for the proton optical potential introduced in the previous Chapter. Both the standard and the modified optical potential was used as input for the statistical model calculations. Perfect agreement was found between the experimental results and the model calculation using the modified JLM potential.

The stellar enhancement factor is given by the ratio of the stellar reaction rate to the ground state reaction rate. This factor — and its uncertainty — is typically much larger when considering a reaction with negative Q value because more excited states can be populated in the target nucleus then in the product, therefore astrophysically relevant transitions are neglected when experimentally studying a reaction with negative Q value. However, we proved that it is possible to derive astrophysical reaction rates for the (n,p) as well as the (p,n) direction from our (p,n) data despite of the negative reaction Q value.

6 Chapter

Proton capture cross sections of ^{106,108}Cd isotopes

6.1 Introduction

Recently, the cross section of the ^{106}Cd(α,γ)^{110}Sn, ^{106}Cd(α,p)^{109}In and ^{106}Cd(α,n)^{109}Sn were measured in the energy range relevant to the p process and compared with statistical model calculations [21]. An elastic α scattering experiment on ^{106}Cd was also carried out, to obtain information on the α-nucleus optical potential [57]. The aim of the present work was to give a complete description of the production of ^{106}Cd p nucleus with taking into account the (γ,p) reactions, too. In order to provide stellar reaction rates, the cross section of the inverse (p,γ) reaction was measured. Moreover, the cross section of the ^{108}Cd(p,γ)^{109}In reaction was also derived

6.2 Investigation of (p,γ) reactions on Cd isotopes

The element Cadmium has eight stable isotopes with mass numbers 106, 108, 110, 111, 112, 113, 114 and 116. The two lightest isotopes, the ^{106}Cd and the ^{108}Cd are p isotopes. Their natural isotopic abundances are 1.25% and 0.89%, respectively. In Table 6.1 the details of the proton induced reactions on the p isotopes of the Cadmium are summarised.

6.1. Table: Proton-induced reactions on proton-rich Cadmium isotopes.

target nucleus	reaction	product nucleus	limitation
^{106}Cd	(p,γ)	^{107}In	no
	(p,γ)	^{107m}In	$T_{1/2} = 50.4$ s
	(p,n)	^{106}In	Threshold (7.38 MeV)
^{108}Cd	(p,γ)	^{109}In	no
	(p,γ)	^{109m_1}In	$T_{1/2} = 80.4$ s
	(p,γ)	^{109m_2}In	$T_{1/2} = 0.21$ s
	(p,n)	^{108}In	Threshold (5.99 MeV)

The primary aim of the present experiment was to measure the proton-induced cross sections of the *p* isotopes. Using the previously discussed activation method, it was possible to measure the cross section of both the ^{106}Cd(p,γ)^{107}In and the ^{108}Cd(p,γ)^{109}In reactions in a single activation experiment. Since the natural isotopic abundances are very low, for having sufficient γ-yield, enriched targets were used at low energies (see Table 6.3 and Table 6.4). As a consequence, this way the number of measurable reactions was limited to the ones, summarized in Table 6.1 except at the higher energy irradiations where natural Cadmium targets were used. However, in this case the low (p,n) thresholds (1.66 MeV for ^{111}Cd(p,n)^{111}In, 3.40 MeV for ^{112}Cd(p,n)^{112}In and 2.25 MeV for ^{114}Cd(p,n)^{114}In reaction, respectively) limits the number of reactions which can be studied with activation since a (p,γ) reaction on Cadmium isotope with mass number A and a (p,n) reaction on a Cadmium isotope with mass number A+1 lead to the same product nucleus. Note, that (p,α), (p,2α), etc. reactions are energetically possible, however their cross sections are orders of magnitude lower (typically 10^{-13} - 10^{-6} barn in the investigated energy region). Therefore γ transitions corresponding to these reactions were not observable in the γ spectra. It was also not possible to measure the cross section of ^{110}Cd(p,n) reaction because the threshold is 4.7 MeV (which is above the investigated energy

6.2. Table: Decay parameters of ^{106,108}Cd(p,γ)^{107,109}In reaction products taken from the literature [84, 85].

Residual nucleus	Half-life [min]	Gamma energy [keV]	Relative γ-intensity per decay [%]
^{107}In	32.4 ± 0.3	204.97 ± 0.03	47.2 ± 0.3
^{109}In	250.0 ± 1.1	203.50 ± 0.02	73.5 ± 0.5

region) and the ^{116}Cd(p,n) because the γ-transitions have low relative intensity. Consequently, here the results of the cross section measurements of the ^{106,108}Cd(p,γ)^{107,109}In reactions are presented below.

Proton capture reactions on ^{106,108}Cd isotopes leads to unstable In isotopes, which decay by β^+ or electron capture to ^{107,109}Cd. For both isotopes the β-decay is followed by γ-radiation which makes possible to determine the proton-capture cross section using the activation method. Table 6.2 summarizes the decay parameters of the reaction products taken from the literature [84, 85]. Only the strongest γ transitions used for the analysis are listed. Since the uncertainty of the ^{109}In half-life is unusually large (2.4%), a half life measurement was also carried out [88] and for the analysis the weighted average of the presently derived half life and the one taken from the literature [88-90] was used.

Both produced In isotopes have metastable states. The proton capture on Cd can populate the ground as well as the metastable states in In. However, in both cases, the metastable states decay exclusively by internal transition to the ground state and the half-lives of the metastable states are short ($T_{1/2} = 50.4$ s for ^{107m1}In, $T_{1/2} = 0.21$ s for ^{109m1}In and $T_{1/2} = 80.4$ s for ^{109m2}In — see table 6.1). Therefore, after a suitable waiting time between the irradiation and the γ-counting, the metastable states have decayed completely to the ground states and hence the measurement of the ground state decay provides information about the total capture cross-section. Figure 6.1 shows the decay scheme of ^{107,109}In.

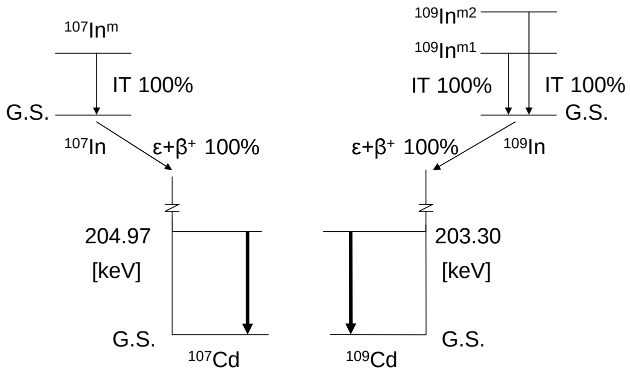

6.1. Figure: Decay scheme of ^{106,108}Cd(p,γ)^{107,109}In reaction products [76, 84, 85]. The γ transitions used for the analysis are indicated.

6.2.1 Target production and irradiation

The same experimental setup was used for the irradiation which was discussed in Chapter 4. The targets were produced with the evaporation of natural as well as highly enriched (96.47% for the ^{106}Cd and 2.05% for the ^{108}Cd) ^{106}Cd powder onto Al foils (see Fig. 5.4 for the schematic view of the evaporation setup). The distance between the backing and the crucible was 5 cm. Using this distance one can still assume that the evaporated layer is homogeneous. The thickness of the targets was measured by weighing (for details, see Chapter 4). At $E_p = 3.2$ MeV and 4.7 MeV the irradiations were carried out both with natural and enriched targets, verifying the ratio of the enrichment. Reasonable agreement was found with the value given by the supplier.

The energy range from $E_p = 2.4$ to 4.7 MeV was covered in 200 keV steps using the Van de Graaff accelerator in the lower and the cyclotron in the upper part of the energy range. The $E_p = 3.0$ MeV and 3.6 MeV irradiations were carried out with both accelerators and no difference in the cross section was found (see below). Each irradiation lasted about 10 h with a beam current of 700 nA. To measure the number of incident particles — similarly to the previously discussed experiments - a current integrator was

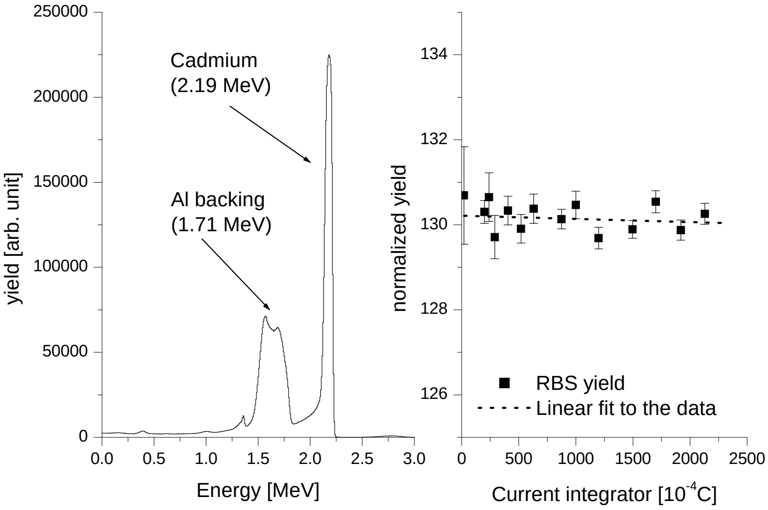

6.2. Figure: Typical RBS spectrum used for monitoring the target stability (left panel). The energy of the beam was 2.4 MeV with beam current of approximately 750 nA and the thickness of the target was 595 μg/cm^2. The right panel shows the yield in the RBS detector normalized to the collected charge as the function of the counts in the current integrator. A linear fit to the measured values is shown and proves that the target deterioration was less than 1%.

used in multichannel scaling mode, stepping a channel in every 10 seconds. The target stability was monitored by detecting the backscattered protons from the Cd target (see Fig. 4.3 for the schematic view of the irradiation setup). The left panel of Fig 6.2 shows a typical RBS spectrum and on the right panel the yield of the RBS detector normalized to the collected charge is shown as the function of the current integrator counts. The dashed line is a fit to the measured values, which proves that the target deterioration was less than 1% (which is taken into account in the uncertainty of the number of target atoms).

6.2.2 Gamma-counting and results

The induced γ-activity of the targets were measured with a calibrated HPGe detector equipped with 5 cm thick lead shielding. More details about the γ-counting setup and the calibration of the detector can be found in Chapter 4. The γ-spectra were taken for at least 10 h to follow the decay of both produced In isotopes. The strongest γ-radiations from the decay of the two In isotopes are very close to each other in energy (203.50 and 204.97 keV). However, the energy resolution of the HPGe detector at this low energy is about 0.8 keV (FWHM); hence the two peaks could be resolved. Moreover, the different half-lives of the two reaction products make the separation even easier. At the beginning of the counting period the 204.96 keV peak from ^{107}In decay dominates, while toward the end of the 10 h counting time this isotope has already decayed and the 203.50 keV peak from ^{107}In decay remains (see Fig. 6.3).

The measured cross sections vary between 3.71 - 1918 μbarn for the reaction ^{106}Cd(p,γ) and between 3.46 - 4733 μbarn for the reaction ^{108}Cd(p,γ). Tables 6.3 and 6.4 list the experimental results for both reactions in the form of effective energies, cross sections as well as astrophysical S factors. There is a good agreement between points measured at similar energies, but with different targets (natural or enriched) or different accelerators.

The quoted uncertainty in the $E_{c.m.}$ values corresponds to the energy

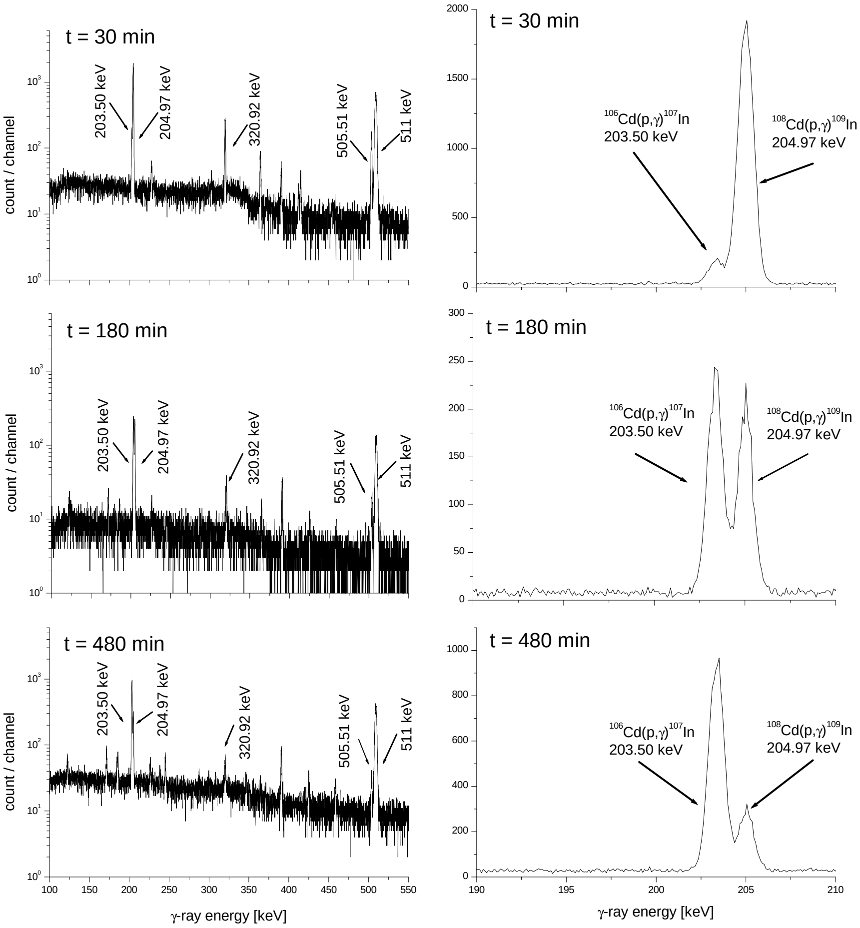

6.3. Figure: Typical γ-spectrum taken 30, 180 and 480 min. after the irradiation of natural Cd target with a 3.8 MeV proton beam (left). The counting time was 30 minute in all cases. The right panel shows the resolved E_γ = 203.50 and 204.97 keV γ-peaks used for the analysis. Other peaks coming from the decay of ^{107}In are also marked, however, these transitions have lower branching ratios and therefore their yield was not always sufficiently high for the analysis. The spectra were erased and the counting was restarted after 120 min.

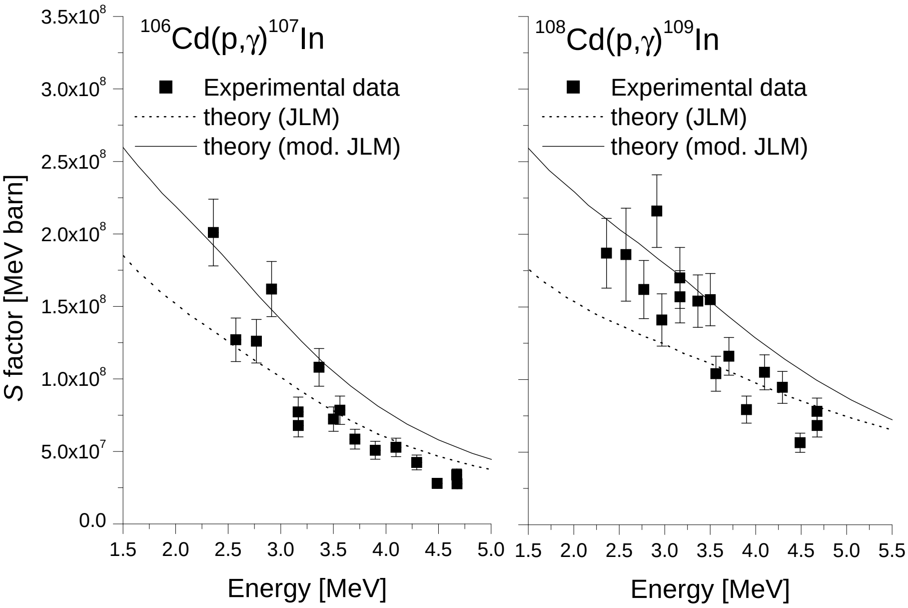

6.4. Figure: Astrophysical S factor as the function of proton energy for the reactions ^{106}Cd(p,γ)^{107}In (left) and ^{108}Cd(p,γ)^{109}In (right) compared to NON-SMOKER calculations using the optical potentials of [71, 72] (JLM) and a modified JLM potential with an increased imaginary strength [52] (for more details, see text).

6.3. Table: Experimental cross sections and S factor values of the ^{106}Cd(p,γ)^{107}In reaction. Since both the Van de Graaff (V) and cyclotron (C) accelerators were used and targets made of enriched (E) as well as natural (N) Cadmium were used therefore in the second column these features of the irradiation are indicated.

$E_{c.m.}$ $[MeV]$	accelerator and target	Cross section $[\mu barn]$	S-factor $[10^6 MeV barn]$
2.359 ± 0.003	V, E	3.71 ± 0.43	201 ± 23
2.573 ± 0.003	V, E	7.96 ± 0.95	127 ± 15
2.769 ± 0.003	V, E	21.2 ± 2.5	126 ± 15
2.913 ± 0.009	C, E	52.9 ± 6.1	162 ± 19
3.166 ± 0.003	V, N	71.5 ± 9.5	77.2 ± 10.3
3.168 ± 0.003	V, E	63.3 ± 7.3	67.8 ± 7.8
3.364 ± 0.003	V, N	209 ± 26	108 ± 13
3.501 ± 0.011	C, E	223 ± 26	72.3 ± 8.4
3.562 ± 0.004	V, N	295 ± 37	78.4 ± 9.8
3.706 ± 0.011	C, E	346 ± 40	58.5 ± 6.8
3.899 ± 0.012	C, N	528 ± 64	50.8 ± 6.2
4.096 ± 0.012	C, N	936 ± 114	52.8 ± 6.4
4.293 ± 0.013	C, N	1232 ± 149	42.4 ± 5.1
4.488 ± 0.014	C, N	1283 ± 155	27.9 ± 3.4
4.674 ± 0.014	C, N	2329 ± 280	33.8 ± 4.1
4.676 ± 0.014	C, E	1918 ± 221	27.7 ± 3.2

stability of the proton beam and to the uncertainty of the energy loss in the target. The uncertainty of the cross-section values is the quadratic sum of the following partial errors: efficiency of the HPGe detector (6%), uncertainty of the level parameters ($\leq$ 0.5%), number of target atoms (6%), current measurement (3%) and counting statistics ($\leq$ 12%).

6.3 Conclusions

The measured astrophysical S factors — plotted in Fig. 6.4 are compared to the results of a Hauser-Feshbach statistical model calculation performed with the NON-SMOKER code [60] using standard (JLM) and modified optical potential (mod JLM). In the case of using JLM potential the agreement between experiment and theory within the measured energy range for the reaction ^{106}Cd(p,γ)^{107}In is good. There is also a reasonable agreement in the case of ^{108}Cd(p,γ)^{109}In for energies above 3.5 MeV, whereas there seems to be a systematic underprediction below that energy. However, it is still well within the usual 30% error which has to be assigned to the global model [31]. Although below 3.5 MeV the ^{108}Cd data are systematically higher than the calculations, no correlation with either the used targets or the type of accelerator was found.

From Fig. 6.4 it might be implied that the energy dependence of the theoretical S factor may be slightly too flat. A stronger increase toward lower energies would better describe the measured values for both reactions. The calculated cross sections and S factors mainly depend on the proton- and γ-strengths. In order to study the sensitivity, we have performed calculations to study the impact of a variation of the strengths by a factor of 2. The results are shown in Fig. 6.5. The plotted sensitivity can have values between 0 and 1, ranging from no impact to a factor of 2 change in the cross section and S factor. It can be seen that the S factors of both reactions are more sensitive to the proton strengths than the γ-strengths across the measured energy range. This is due to the Coulomb suppression of the proton-widths at such low energies. Consequently, a change in the nuclear

6.4. Table: Experimental cross sections and S factor values of the ^{108}Cd(p,γ)^{109}In reaction. Since both the Van de Graaff (V) and cyclotron (C) accelerators were used and targets made of enriched (E) as well as natural (N) Cadmium were used therefore in the second column these attributes of the irradiation are indicated.

$E_{c.m.}$ $[MeV]$	accelerator and target	Cross section $[\mu barn]$	S-factor $[10^6 MeV barn]$
2.360 ± 0.003	V, E	3.46 ± 0.45	187 ± 24
2.573 ± 0.003	V, E	11.6 ± 2.0	186 ± 32
2.770 ± 0.003	V, E	27.3 ± 3.3	162 ± 20
2.913 ± 0.009	C, E	70.0 ± 8.1	216 ± 25
2.968 ± 0.003	V, N	58.0 ± 7.4	141 ± 18
3.166 ± 0.003	V, N	157 ± 19	170 ± 21
3.168 ± 0.003	V, E	146 ± 17	157 ± 18
3.365 ± 0.003	V, N	298 ± 35	154 ± 18
3.505 ± 0.011	C, E	482 ± 57	155 ± 18
3.563 ± 0.004	V, N	391 ± 45	104 ± 12
3.706 ± 0.011	C, E	686 ± 79	116 ± 13
3.900 ± 0.012	C, N	825 ± 97	79.3 ± 9.3
4.097 ± 0.012	C, N	1862 ± 219	105 ± 12
4.293 ± 0.013	C, N	2744 ± 322	94.6 ± 11
4.489 ± 0.014	C, N	2592 ± 304	56.5 ± 6.6
4.675 ± 0.014	C, N	5392 ± 633	78.1 ± 9.2
4.677 ± 0.014	C, E	4733 ± 545	68.3 ± 7.9

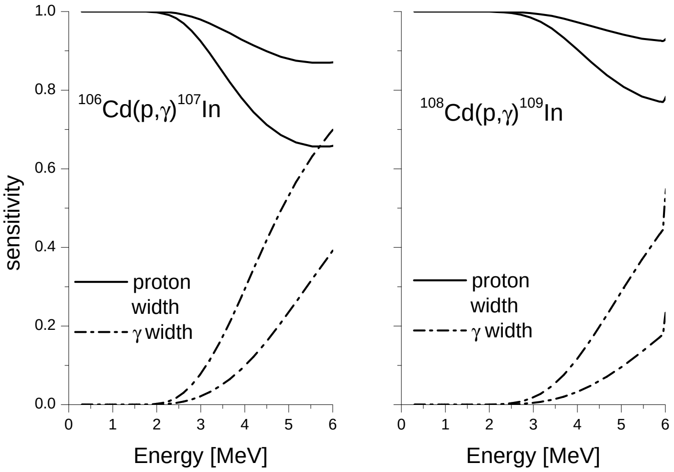

6.5. Figure: Sensitivity of the ^{106}Cd(p,γ)^{107}In (left) and ^{106}Cd(p,γ)^{107}In (right) reaction cross sections to a variation in the proton- and γ-strengths as a function of the c.m. energy. The sensitivity ranges from 0 (no change) to 1 (the cross section changes by the same factor as the strength).

properties determining the γ-strength would only have a limited impact and only at the high end of the measured range as can be seen on Fig. 6.5.

The impact would be larger for ^{108}Cd(p,γ)^{109}In than for the other reaction. The E1 Giant Dipole Resonance strength function and the nuclear level density in the compound nucleus determine the γ-strength, whereas the main property for the proton width is the optical potential for protons. The standard calculation shown here uses E1 and M1 transmission coefficients as described in [30], the nuclear level density of [31] and the microscopic JLM proton optical potential as discussed in Chapter 4.

Since in the sensitivity study we found that the cross section depends crucially on the proton-width computed from the proton optical potential, another model calculation was performed using the modified JLM potential (for details of this potential, see Chapter 4). It was found that the slope of the calculated S factor is steeper in both reactions as can be seen in Fig. 6.4 (full line). The energy dependence of theoretical calculations using

6.5. Table: Astrophysical reaction rates of the reaction ^{106}Cd(p,γ)^{107}In computed from the experimental data.

Temperature [10^9 K]	Reaction Rate [cm^{3}s^{-1}mole^{-1}]
2.50	$(1.78\pm0.22)\times10^0$
2.75	$(5.66\pm0.70)\times10^0$
3.00	$(1.52\pm0.19)\times10^1$
3.25	$(3.56\pm0.44)\times10^1$
3.50	$(7.47\pm0.93)\times10^1$
3.75	$(1.43\pm0.18)\times10^2$

the modified JLM potential agrees better with the measured cross sections, however, the theory still overestimates slightly the experimental data. This can be due to large γ width. Toward higher energies, the S factor becomes more and more sensitive to the γ width. Reducing it would reduce the calculated S factor more strongly at higher energies than at lower ones.

The crucial quantity important for the application in astrophysical models is the astrophysical reaction rate. Because of the limited energy range of the data, the relevant integration can only be performed for a limited range of temperatures when adopting an upper limit for the error in the integration due to the energy cutoff. For the derivation of the astrophysical reaction rates from the data, we used the code EXP2RATE [73] which automatically determines the possible temperature window and also accounts for the experimental error. Allowing an error of 15%, we find that the covered temperature range is (2.5-3.75) x 10^9 K for ^{106}Cd(p,γ)^{107}In and (2.5-3.5) x 10^9 K for ^{108}Cd(p,γ)^{109}In. This covers well the relevant p-process temperature range which is usually given as (2.0-3.0) x 10^9 K. The resulting rates with their experimental errors are given in Table 6.5 and Table 6.6.

6.6. Table: Astrophysical reaction rates of the reaction ^{108}Cd(p,γ)^{109}In computed from the experimental data.

Temperature [10^9 K]	Reaction Rate [cm^{3}s^{-1}mole^{-1}]
2.50	$(2.56\pm0.34)\times10^0$
2.75	$(8.42\pm1.10)\times10^0$
3.00	$(2.33\pm0.30)\times10^1$
3.25	$(5.60\pm0.73)\times10^1$
3.50	$(1.20\pm0.16)\times10^2$

6.4 Summary

The proton-capture cross sections of the two *p* isotopes of Cadmium were measured in the astrophysically relevant energy region for the *p* process using the activation technique. The experimental results were compared to statistical model calculations performed with the NON-SMOKER code with standard input parameters.

Since a difference between the energy-dependence of the measured and the calculated *S* factors were found, a sensitivity study was carried out, to investigate the behavior of the statistical model calculation when varying the nuclear inputs like proton and γ widths. It was found that the cross section of both reactions depends more sensitively on the proton widths computed from the proton optical potential in the measured energy range, than on the γ widths.

Moreover, we repeated the model calculations using the modified JLM potential with increased imaginary strength. This case, better agreement between the energy dependence of the measured and the calculated data was found, however it seems that the theory overestimates the *S* factors. A detailed study on the effects of the variation of the γ width on the calculated cross sections is needed.

7 Chapter

Summary

This thesis is based on experimental works in the field of nuclear astrophysics. Between 2004 and 2008 I have been involved in several different research activities dealing with nuclear reactions relevant for the so-called astrophysical *p* process. The *p* process is the mechanism synthesizing the proton rich heavy nuclei (*p* nuclei) that cannot be produced via neutron capture. This process involves several sub-processes, however the key role is played by a chain of (γ,n) reactions followed by (γ,p) and (γ, α) photodisintegrations. The (γ,p) reactions are more important for the synthesis of the light (A $\leq$ 100), while the (γ, α) reactions are crucial for the case of the heavy *p* nuclei. The experimental investigation of these γ-induced reactions is technically difficult (or impossible), however, the inverse reactions can provide useful indirect information. Moreover it was stated recently that certain (p,n) and (n,p) reactions on *s* or *r* seed nuclei can affect the *p* abundances. For these reasons the cross sections of the ^{70}Ge(p,γ)^{71}As, ^{76}Ge(p,n)^{76}As, ^{85}Rb(p,n)^{85}Sr and ^{106,108}Cd(p,γ)^{107,109}In reactions have been measured in this work using the activation technique.

The details of those subjects can be found in the thesis, where my contribution was essential. In all cases the motivation of the work, the experimental procedures as well as the results are reviewed.

All experiments were performed using the Van de Graaff and cyclotron accelerators of ATOMKI. The targets were produced by evaporation natural Germanium, Rubidiumchloride and natural as well as enriched ^{106}Cd metallic powder onto thin Al foils. The number of target atoms were derived by weighing assuming that the evaporated layer is homogeneous. The energy of the proton beam was between 1.6 - 4.4 MeV covered in 400 keV steps and 2.2 - 4.0 MeV covered in 200 keV steps for the ^{70}Ge(p,γ)^{71}As, ^{76}Ge(p,n)^{76}As reactions and for the ^{85}Rb(p,n)^{85}Sr, ^{106,108}Cd(p,γ)^{107,109}In reactions, respectively. The cross sections were determined in the astrophysically relevant energy region from the yield of the induced γ-radiation following the decay of the reaction products, which was detected by a calibrated HPGe detector. The experimental results were compared to statistical model calculations. In all cases astrophysical reaction rates at the relevant temperatures are also provided.

- The cross sections of ^{70}Ge(p,γ)^{71}As and ^{76}Ge(p,n)^{76}As reactions were measured with a precision better than 12% in the astrophysically relevant energy region. The resulted cross sections were compared to statistical model calculations using standard proton optical potential as input. It was found that there is a difference between the slope of the measured values and the theoretical predictions. Therefore a sensitivity calculation was carried out to investigate the behavior of the theoretical cross section as the function of nuclear inputs like proton, neutron and γ widths. Since it was found that the cross sections depend sensitively on the proton-widths computed from the proton optical potential, to describe better the experimental data, we suggested to modify the imaginary part of the potential by increasing its strength by 70%. The cross sections of the previous (p,γ) and (p,n) studies were compared to the statistical model calculations using the modified potential and better agreement between the experimental data and the theoretical calculations were found. Astrophysical reaction rates are also computed from the experimental data.

- It was reported that the p abundances derived from network calculations are particularly sensitive to the cross section of the ^{85}Rb(p,n)^{85}Sr reaction. The experimental data existing at the relevant energy region have large uncertainties both in the c.m. energy and in the cross section. The aim of this work was to provide high precision data at these energies and compare the experimental results with calculated cross sections using the previously discussed improved optical potential. The number of target atoms were derived using Rutherford Backscattering Spectroscopy too. Using this method it was also proved that the evaporated RbCl layer is flat and the Rb to Cl ratio is constant. Since the half life of the ^{85}Sr is relatively long, the activity measurement was carried out not only after the irradiation but also approximately one month later. The cross sections were calculated from the average weighted by the statistical uncertainty of the two independent γ-counting. The results were compared to statistical model calculations using the improved potential derived from our previous work and perfect agreement were found. Moreover, it was shown that in this case it is possible to derive astrophysical reaction rates for the (n,p) as well as the (p,n) reaction from the measured ^{85}Rb(p,n)^{85}Sr cross section data despite the negative reaction Q value.

- In this work, the cross section of the ^{106,108}Cd(p,γ)^{107,109}In reactions were measured. Different accelerators and targets were used therefore several overlapping irradiations were done. Since a difference between the measured and the calculated S factors were found, therefore, a sensitivity study was carried out, to investigate the behavior of the statistical model calculation when varying the nuclear inputs like proton and γ widths. It was found that the cross section of both reactions depends sensitively on the proton widths computed from the proton optical potential at the measured energies. Moreover, we repeated the model calculation using our modified proton optical potential. It was found that the results of these calculations can describe better the energy dependence of the experimental data, however it seems that the theory is still slightly overestimating the S factors.

8 Chapter

Összefoglalás

Disszertációm tárgyát a kísérleti nukleáris asztrofizika területén végzett munkám képezi. 2004 és 2008 között számos különböző hatáskeresztmetszet mérésben vettem részt, melyekben közös, hogy az úgynevezett asztrofizikai *p* folyamat vizsgálatához kapcsolódnak. A *p* folyamat során azon nehéz, protongazdag izotópok keletkeznek melyek nem jöhetnek létre neutronbefogás révén. Számos egyéb folyamat ad járulékot a *p* magok naprendszerbeli gyakoriságához, azonban a kulcsszerepet a (γ,n) fotobomlások és az azokat követő (γ, α) és (γ,p) reakciók játszák. A (γ,p) reakciók a könnyebb (A $\leq$ 100), míg a (γ, α) reakciók az ezeknél nehezebb *p* magok keletkezésében meghatározóak. A fotobomlási reakciók a jelen technikai körülmények között nehezen vagy egyáltalán nem vizsgálhatók, azonban az inverz reakciók hatáskeresztmetszetének mérésével lényeges közvetett információk nyerhetőek. Továbbá a legújabb elméleti eredmények felhívták a figyelmet arra, hogy neutronbefogás révén keletkezett nehéz magokon lejátszódó (p,n) és (n,p) reakciók lényegesen befolyásolhatják a könnyű *p* magok gyakoriságát. Ezen okokbol a következő reakciók hatáskeresztmetszetét határoztuk meg nagy pontossággal: ^{70}Ge(p,γ)^{71}As, ^{76}Ge(p,n)^{76}As, ^{85}Rb(p,n)^{85}Sr, valamint ^{106,108}Cd(p,γ)^{107,109}In. A méréseket aktivációs technikával végeztük el. Jelen dolgozatban azon eredményeinket ismertetem melyekben meghatározó volt a hozzájárulásom, a vizsgálatok motivációjának, a megvalósítás kísérleti körülményeinek, a nyert eredményeknek és következményeiknek bemutatásával.

A hatáskeresztmetszet méréseket minden esetben az ATOMKI Van de Graaff és ciklotron gyorsítóival végeztük. Céltárgyainkat természetes germánium, rubidiumklorid valamint természetes és ^{106}Cd izotópban dúsított kadmium por vékony Al fóliára való párologtatásával készítettük. A céltárgymagok számát mérlegeléssel határoztuk meg. A protonnyaláb energiája az 1,6 - 4,4 MeV (^{70}Ge(p,γ) és ^{76}Ge(p,n) reakciók) valamint a 2,2 - 4,0 MeV tartományba esett (^{85}Rb(p,n) illetve ^{106,108}Cd(p,γ reakciók) melyet 400 illetve 200 keV-es lépésközökkel térképeztünk fel. A hatáskeresztmetszeteket az asztrofizikai szempontból fontos energiatartományban mértük meg. A hatáskeresztmetszeteket a reakciótermékek bomlását kísérő γ-sugárzás intenzitásának méréséből határoztuk meg. A γ-sugárzás intenzitását HPGe detektorral mértük, melyet radioaktív forrásokkal kalibráltunk. Kísérleti eredményeinket összehasonlítottuk statisztikus modellszámítások jóslataival. A vizsgált reakciók asztrofizikai reakciósebességét szintén meghatároztuk a csillaghőmérsékletnek megfelelő energiatartományban.

- A germánium izotópokon protonbombázás során lejátszódó reakciók vizsgálatát végeztük el nagy pontossággal. A hatáskeresztmetszetek energiafüggésében eltérést tapasztaltunk az elméleti számításokhoz képest. Ezen eltérés okának meghatározására megvizsgáltuk, hogy a statisztikus modellszámítás eredménye hogyan módosul az egyes bemenő paraméterek — úgymint proton, neutron es gamma parciális szélességek — változtatásának hatására. Úgy találtuk, hogy a számítások különösen érzékenyek a proton parciális szélességének változtatására, mely a proton-mag optikai potenciálból származtatható. A kísérleti eredményeket legjobban abban az esetben sikerült leírni, amikor a statisztikus modell számítások bemenő paramétereként egy olyan optikai potenciált használtunk melynek képzetes része 70%-kal haladta meg a korábbi számitásokban használtat. Ezen módosított potenciál használatával elvégeztük a modellszámításokat a korábban mért reakciókra is és pontosabb leírását tudtuk adni az eredményeknek, mint az irodalmi potenciál használatával.

- Elméleti munkák megmutatták, hogy *p* magok gyakorisága jelentősen függ a ^{85}Rb(p,n)^{85}Sr reakció hatáskeresztmetszetétől. Ezen reakció korábbi vizsgálatának eredményei azonban pontatlanok a modellszámítások jóslatainak ellenőrzéséhez, ezért célul tűztük ki a fenti reakció hatáskeresztmetszetének asztrofizikai energiákon történő meghatározását. Továbbá ily módon lehetőségünk nyílik a korábban részletezett módosított optikai potenciál további kísérleti ellenőrzésére. A céltárgymagok számát Rutherford visszaszórási eljárással is meghatároztuk. Ez az eljárás arra is lehetőséget adott, hogy ellenőrizzük a céltárgy felületének egyenletességét valamint a rubidium és klór magok arányát a besugárzás előtt és után. A mért hatáskeresztmetszeteket összehasonlítottuk mind az irodalmi mind a módosított potenciál segítségével számolt elméleti értékekkel és utóbbi esetben jó egyezést találtunk. Ezenkívül megmutattuk, hogy megfelelő feltételek teljesülése esetén a reakció negatív Q értékének ellenére is lehetséges a reakciósebességek meghatározása a csillaghőmérsékletnek megfelelő energiákon mind a direkt, mind az inverz reakció esetén.

- A ^{106,108}Cd(p,γ)^{107,109}In reakciók hatáskeresztmetszetét mértük meg a csillaghőmérsékletnek megfelelő energiákon. Mivel különböző céltárgyakat és gyorsítókat használtunk, számos besugárzást megismételtünk. Az azonos energián különböző gyorsítóval végzett, valamint azonos energián természetes és dúsított céltárgyak besugárzásával mért hatáskeresztmetszetek jó egyezést mutatnak. A kísérleti eredményeink és a statisztikus modellszámítás jóslatai között eltérést találtunk, ezért megvizsgáltuk, hogyan változik a számított hatáskeresztmetszet, ha változtatjuk a bemenő mag-paramétereket. Azt találtuk, hogy — hasonlóan a korábbi esetekhez — a számítás a proton szélességek, következésképpen a proton-mag optikai potenciál változtatására érzékeny. A modellszámításokat elvégeztük az általunk módosított proton optikai potenciál alkalmazásával is. Azt találtuk, hogy az ezen potenciál alkalmazásával elvégzett modellszámítás eredménye jobb egyezésben van a kísérleti adatokkal, azonban kicsit felülbecsüli a mérés eredményeit. Ennek legvalószínűbb oka, hogy a számításokban használt γ szélességek túl nagyok. A γ szélességek változtatásának hatásának vizsgálata részletes további kutatásokat igényel.

Bibliography

[1] E. M. Burbidge, G. R. Burbidge, W. A. Fowler and F. Hoyle, Rev. Mod. Phys. **29**, 547 (1957).

[2] A. Cameron Report CRL-41, A.E.C.L. Chalk River, Canada (1957).

[3] G. Gamow, Z. Phys. **51**, 204 (1928).

[4] R. A. Alpher, H. A. Bethe, G. Gamow, Phys. Rev. **73**, 803 (1948).

[5] R. Diehl, K. Bennett, H. Bloemen, W. Collmar, W. Hermsen, G. G. Lichti, M. McConnell, D. Morris, J. Ryan, V. Schönfelder, H. Steinle, A. W. Strong, B. N. Swanenburg, M. Varendorff and C. Winkler, Advances in Space Research, **13**, 723 (1993).

[6] S. E. Woosley and W. M. Howard, Astrophys. J. Suppl. **36**, 285 (1978).

[7] G. Wallerstein, I. Iben, P. Parker, A. M. Boesgaard, G. M. Hale, A. E. Champagne, C. A. Barnes, F. Käppeler, V. V. Smith, R. D. Hoffman, F. X. Timmes, C. Sneden, R. N. Boyd, B. S. Meyer and D. L. Lambert, Rev. Mod. Phys. **69**, 995 (1997).

[8] C. Rolfs and W. Rodney, Cauldrons in the Cosmos. The University of Chicago Press (1988).

[9] C. Iliadis, *Nuclear physics of Stars*. WILEY-VCH Verlag Gmbh Co. KGaA (2007).

[10] K. Lodders, Astrophys. J **591**, 1220 (2003).

[11] C. Arlandini, F. Käppeler, K. Wisshak, R. Gallino, M. Lugaro, M. Busso and O. Straniero, Astrophys. J. **525**, 886 (1999).

[12] R. Gallino, C. Arlandini, M. Busso, M. Lugaro, C. Travaglio, O. Straniero, A. Chieffi and M. Limongi, Astrophys. J. **497**, 388 (1998).

[13] F. Käppeler, Prog. Part. Nucl. Phys. **43**, 419 (1999).

[14] S. Rosswog, M. Liebendörfer, F.-K. Thielemann, M.B. Davies, W. Benz and T. Piran, Astron. Astrophys. **341**, 499 (1999).

[15] S. E. Woosley, J. R. Wilson, G. J. Mathews, R. D. Hoffmann and B. S. Meyer, Astrophys. J. **433**, 229 (1994).

[16] A. G. W. Cameron, Astrophys. J. **587**, 327 (2003).

[17] K. Takahashi, J. Witti and H.-T. Janka, Astron. Astrophys. **286**, 857, (1994).

[18] M. Arnould, Phys. Lett. **450**, 97 (2007).

[19] T. Motobayashi, Prog. Part. Nucl. Phys. **42**, 37 (1999).

[20] M. Arnould and S. Goriely, Phys. Rep. **384**, 1 (2003).

[21] Gy. Gyürky, G. G. Kiss, Z. Elekes, Zs. Fülöp, E. Somorjai, A. Palumbo, J. Görres, H. Y. Lee, W. Rapp, M. Wiescher, N. Özkan, R. T. Güray, G. Efe and T. Rauscher, Phys. Rev. C **74**, 5805 (2006).

[22] S. E. Woosley, T. S. Axelrod and T. A. Weaver, Comments Nucl. Part. Phys. **9**, 185 (1981).

[23] K. Langanke and M. Wiescher, Rep. Prog. Phys. **64**, 1657 (2001).

[24] H. Schatz, A. Aprahamian, J. Görres, M. Wiescher, T. Rauscher, J. F. Rembges, F. -K. Thielemann, B. Pfeiffer, P. Möller and K. -L. Kratz, Phys. Rep. **294**, 167 (1998).

[25] S. E. Woosley, D. H. Hartmann, R. D. Hoffman and W. C. Haxton, Astrophys. J. **356**, 272 (1990).

[26] C. Fröhlich, G. Martínez-Pinedo, M. Liebendörfer, F.-K. Thielemann, E. Bravo, W. R. Hix, K. Langanke and N. T. Zinner, Phys. Rev. Lett. **96**, 142502 (2006).

[27] T. Rauscher, Phys. Rev. C **73**, 015804 (2006).

[28] W. Rapp, J. Görres, M. Wiescher, H. Schatz and F. Käppeler, Astrophys. J. **653**, 474 (2006).

[29] W. Hauser and H. Feshbach, Phys. Rev. **87**, 366 (1952).

[30] T. Rauscher and F. K. Thielemann, At. Data Nucl. Data Tables **75**, 1 (2000).

[31] T. Rauscher, F.-K. Thielemann and K.-L. Kratz, Phys. Rev. C **56**, 1613 (1997).

[32] P. Mohr, K. Vogt, M. Babilon, J. Enders, T. Hartmann, C. Hutter, T. Rauscher, S. Voltz and A. Zilges, Phys. Lett. B **488**, 127 (2000).

[33] K. Sonnabend, K. Vogt, D. Galaviz, S. Müller and A. Zilges, Phys. Rev. C **70**, 035802 (2004).

[34] H. Utsunomiya, H. Akimune, S. Goko, M. Ohta, H. Ueda, T. Yamagata, K. Yamasaki, H. Ohgaki, H. Toyokawa, Y.-W. Lui, T. Hayakawa, T. Shizuma, E. Khan and S. Goriely, Phys. Rev. C **67**, 015807 (2003).

[35] T. Shizuma, H. Utsunomiya, P. Mohr, T. Hayakawa, S. Goko, A. Makinaga, H. Akimune, T. Yamagata, M. Ohta, H. Ohgaki, Y.-W. Lui, H. Toyokawa, A. Uritani and S. Goriely, Phys. Rev. C **72**, 025808 (2005).

[36] P. Mohr, Zs. Fülöp and H. Utsunomiya, Eur. Phys. J. A **32**, 357 (2007).

[37] Zs. Fülöp, Á.Z. Kiss, E. Somorjai, C.E. Rolfs, H.P. Trautvetter, T. Rauscher and H. Oberhummer, Z. Phys. A **355**, 203 (1996).

[38] W. Rapp, H.J. Brede, M. Heil, D. Hentschel, F. Käppeler, H. Klein, R. Reifarth and T. Rauscher, Nucl. Phys. **A688**, 427 (2001).

[39] N. Özkan, G. Efe, R. T. Güray, A. Palumbo, M. Wiescher, J. Görres, H. Y. Lee, Gy. Gyürky, Zs. Fülöp and E. Somorjai, Phys. Rev. C **75**, 5801 (2007).

[40] E. Somorjai, Zs. Fülöp, Á.Z. Kiss, C.E. Rolfs, H.P. Trautvetter, U. Greife, M. Junker, S. Goriely, M. Arnould, M. Rayet, T. Rauscher and H. Oberhummer, Astron. Astrophys. **333**, 1112 (1998).

[41] C. E. Laird, D. Flynn, R. L. Hershberger and F. Gabbard, Phys. Rev. C **35**, 1265 (1987).

[42] T. Sauter and F. Käppeler, Phys. Rev. C **55**, 3127 (1997).

[43] J. Bork, H. Schatz, F. Käppeler and T. Rauscher, Phys. Rev. C **58**, 524 (1998).

[44] F. R. Chloupek, A. StJ. Murphy, R. N. Boyd, A. L. Cole, J. Görres, R. T. Guray, G. Raimann, J. J. Zach, T. Rauscher, J. V. Schwarzenberg, P. Tischhauser and M. C. Wiescher, Nucl. Phys. **A652**, 391 (1999).

[45] Gy. Gyürky, E. Somorjai, Zs. Fülöp, S. Harissopulos, P. Demetriou and T. Rauscher, Phys. Rev. C **64**, 065803 (2001).

[46] S. Harissopulos, E. Skreti, P. Tsagari, G. Souliotis, P. Demetriou, T. Paradellis, J. W. Hammer, R. Kunz, C. Angulo, S. Goriely and T. Rauscher, Phys. Rev. C **64**, 055804 (2001).

[47] N. Özkan, A. StJ. Murphy, R. N. Boyd, A. L. Cole, M. Famiano, R.T. Güray, M. Howard, L. Sahin, J.J. Zach, R. deHaan, J. Görres, M. C. Wiescher, M.S. Islam and T. Rauscher, Nucl. Phys. **A710**, 469 (2002).

[48] S. Galanopoulos, P. Demetriou, M. Kokkoris, S. Harissopulos, R. Kunz, M. Fey, J. W. Hammer, Gy. Gyürky, Zs. Fülöp, E. Somorjai and S. Goriely, Phys. Rev. C **67**, 015801 (2003).

[49] Gy. Gyürky, Zs. Fülöp, E. Somorjai, M. Kokkoris, S. Galanopoulos, P. Demetriou, S. Harissopulos, T. Rauscher and S. Goriely, Phys. Rev. C **68**, 055803 (2003).

[50] P. Tsagari, M. Kokkoris, E. Skreti, A. G. Karydas, S. Harissopulos, T. Paradellis and P. Demetriou, Phys. Rev. C **70**, 015802 (2004).

[51] Gy. Gyürky, G. G. Kiss, Z. Elekes, Zs. Fülöp, E. Somorjai and T. Rauscher, Eur. Phys. J. **27**, 141 (2006).

[52] G. G. Kiss, Gy. Gyürky, Z. Elekes, Zs. Fülöp, E. Somorjai, T. Rauscher and M. Wiescher, Phys. Rev. C **76**, 055807 (2007).

[53] M. A. Famiano, R. S. Kodikara, B. M. Giacherio, V. G. Subramanian and A. Kayani, Nucl Phys. A **802**, 26 (2008).

[54] P. Mohr, T. Rauscher, H. Oberhummer, Z. Máté, Zs. Fülöp, E. Somorjai, M. Jäger and G. Staudt, Phys. Rev. C **55**, 1523 (1997).

[55] Zs. Fülöp, Gy. Gyürky, Z. Máté, E. Somorjai, L. Zolnai, D. Galaviz, M. Babilon, P. Mohr, A. Zilges and T. Rauscher, Phys. Rev. C **64**, 065805 (2001).

[56] D. Galaviz, Zs. Fülöp, Gy. Gyürky, Z. Máté, P. Mohr, T. Rauscher, E. Somorjai E and A. Zilges, Phys. Rev. C **71**, 065802 (2005).

[57] G. G. Kiss, Zs. Fülöp, Gy. Gyürky, Z. Máté, E. Somorjai, D. Galaviz, A. Kretschmer, K. Sonnabend and A. Zilges, Eur. Phys. J. **A27**, 197 (2006).

[58] G. G. Kiss, Gy. Gyürky, Zs. Fülöp, E. Somorjai, D. Galaviz, A. Kretschmer, K. Sonnabend, A. Zilges, P. Mohr and M. Avrigeanu, J. Phys. G. **35**, 014037 (2007).

[59] D. Galaviz *et al.*, in preparation.

[60] T. Rauscher and F.-K. Thielemann, in *Stellar Evolution, Stellar Explosions, and Galactic Chemical Evolution*, ed. A. Mezzacappa (IOP, Bristol 1998), p. 519.

[61] http://www-nds.iaea.org/exfor/exfor00.htm

[62] I. Dillmann, M. Heil, F. Käppeler, R. Plag, T. Rauscher and F.-K. Thielemann, AIP Conf. Proc. **819**, 123 (2006).

[63] http://nuclear-astrophysics.fzk.de/kadonis

[64] http://www.nndc.bnl.gov

[65] M. R. Bhat, Nuclear Data Sheets **68**, 579 (1993).

[66] B. Singh, Nuclear Data Sheets **74**, 63 (1995).

[67] J. F. Ziegler and J. P. Biersack, code SRIM Version 2003.20 (2003).

[68] S. Agostinelli J. Allison, K. Amako, J. Apostolakis, H. Araujo, P. Arce, M. Asai, D. Axen, S. Banerjee and G. Barrand, Nucl. Instr. Meth. A **506**, 250 (2003).

[69] K. Debertin and U. Schötzig Nucl. Instr. and Meth. **158**, 471 (1979).

[70] T. Rauscher and F. K. Thielemann, At. Data Nucl. Data Tables **79**, 47 (2001).

[71] J. P. Jeukenne, A. Lejeune and C. Mahaux, Phys. Rev. C **16**, 80 (1977).

[72] A. Lejeune, Phys. Rev. C **21**, 1107 (1980).

[73] T. Rauscher, code EXP2RATE (2003), http://download.nucastro,org/codes/exp2rate.f

[74] N. A. Roughton, M. R. Fritts, R. J. Petersen, C. S. Zaidins and C. J. Hansen, At. Data Nucl. Data Tables **23**, 177 (1979).

[75] H. Siever, Nucl. Data Sheets **62**, 271 (1991).

[76] http://nucleardata.nuclear.lu.se

[77] A. Simon, T. Csákó, C. Jeynes and T. Sörényi, Nucl. Instr. Meth. **B249**, 454 (2006).

[78] Zs. Kertész, A. Simon, Z. Szikszai, R. Huszánk, E. Dobos, G. Szíki, Á. Z. Kiss and I. Uzonyi Conference on Particle-Induce X-ray Emission and its Analytical Applications. Puebla, Mexico, 25-29 May, 2007. Proceedings. Eds.: Miranda, J., Ruvalcaba-Sil, J.L., de Lucio, O.G. Mexico City, Universidad Nacional Autónoma de México (CD), 12 (2007).

[79] Zs. Kertész, Z. Szikszai, I. Uzonyi, A. Simon and Á. Z. Kiss, Nucl. Instr. Meth. **B231**, 106 (2005).

[80] Zs. Kertész, Z. Szikszai, E. Gontier, P. Moretto, J. E. Surleve-Bazeille, B. Kiss, I. Juhász, J. Hunyadi and Á. Z. Kiss, Nucl. Instr. Meth. **B231**, 280 (2005).

[81] E. Kótai, Nucl. Instr. Meth. **B85**, 588 (1994).

[82] S.Kastleiner, S.M.Qaim, F.M.Nortier, G.Blessing, T.N.van der Walt and H.H.Coenen, Appl. Radiat. Isot. **56**, 685 (2002).

[83] T. Rauscher, http://nucastro.org/nosmo.html

[84] J. Blanchot, Nuclear Data Sheets **89**, 213 (2000).

[85] J. Blanchot, Nuclear Data Sheets **107**, 355 (2006).

[86] D. De Frenne and E. Jacobs, Nuclear Data Sheets **89**, 481 (2000).

[87] D. R. Tilley, C. M. Cheves, J. L. Godwina, G. M. Hale, H. M. Hofmann, J. H. Kelley, C. G. Sheu and H. R. Weller, Nucl. Phys. A **708**, 3 (2002).

[88] Gy. Gyürky, Z. Elekes, Zs. Fülöp, G. G. Kiss, E. Somorjai, A. Palumbo and M. Wiescher, Phys. Rev. C **71**, 057302 (2005).

[89] E. C. Mallary and M. L. Pool, Phys Rev. **76**, 1454 (1949).

[90] C. L. McGinnis, Phys. Rev. **81**, 734 (1951).

[91] M. Nozawa, Nucl. Phys. A **37**, 411 (1962).

Acknowledgment

In this thesis I have reported on the work I have made during my Ph.D. course. During these years I have enjoyed the help and the teaching of many people, who have made possible the theses itself. Therefore its my duty, besides my pleasure, to thank all of them at the end of this experience.

First of all, I would like to thank for the directors of ATOMKI, R. Lovas and Zs. Fülöp for providing the working conditions for me. I would like to thank my supervisor E. Somorjai for introducing me to nuclear astrophysics. His support and guidance are fully acknowledged. I am very grateful to him for his continuous help and encouragement.

In the every day work I got enormous help from Gy. Gyürky. I would like to thank him this. I have to thank also the help I got from all workers of the Department of Electrostatic Accelerators. I would like also acknowledge that E. Somorjai, Zs. Fülöp, Gy. Gyürky, D. Bemmerer and P. Mohr read and corrected my thesis.

I would like to acknowledge the work of the engineers and operators of both the Van de Graaff and cyclotron accelerators (L. Bartha, P. Kovács, Z. Kormány, J. Szitta, S. Török, L. Márta, J. Szathmári, L. Buday, I. Erdődi, L. Juhos, S. Kulcsár, E. Madarász).

For providing the theoretical calculations I would like to thank the work of T. Rauscher.

I would like to acknowledge the nice years I spent here for every workers at ATOMKI, especially for the players of the soccer team (G. Lévai, G. Székely, Zs. Mezei, Zs. Kertész, Zs. Fülöp, E. Somorjai, Z. Elekes, I. Futó, G. Kiss, I. Csige, Gy. Pósán) and the players of the ulti - group (Z. Balogh, L. Csige and Z. Palánki) for making my days colorful.

Finally, I would like to thank the support and help I got from my parents and my grandfather.

9 Chapter

Publications

Publications related to the PhD thesis

1. Gy. Gyürky, **G. G. Kiss**, Z. Elekes, Zs. Fülöp and E. Somorjai,
   ^{106,108}Cd(p,γ)^{107,109}In cross sections for the astrophysical p process,
   European Physical Journal A **27**, 141 (2006).

2. **G. G. Kiss**, Gy. Gyürky, Z. Elekes, Zs. Fülöp, E. Somorjai, T. Rauscher and M. Wiescher,
   ^{70}Ge(p,γ)^{71}As and ^{76}Ge(p,n)^{76}As cross sections for the astrophysical p process: Sensitivity of the optical proton potential at low energies,
   Physical Review C **76**, 505807 (2007).

3. Gy. Gyürky, **G. G. Kiss**, Z. Elekes, Zs. Fülöp, E. Somorjai and T. Rauscher,
   Proton capture cross-section of ^{106,108}Cd for the astrophysical p-process,
   Journal of Physics G **34** 817 (2007).

4. **G. G. Kiss**, Gy. Gyürky, Z. Elekes, Zs. Fülöp, E. Somorjai, T. Rauscher and M. Wiescher,
   Investigation of proton-induced reactions on Germanium isotopes,
   Journal of Physics G **35**, 4032 (2008).

5. **G. G. Kiss**, Gy. Gyürky, A. Simon, Zs. Fülöp, E. Somorjai and T. Rauscher,
Coulomb suppression of the stellar enhancement factor and experimental determination of the astrophysical reaction rate of $^{85}Rb(p,n)^{85}Sr$ *for the p process*,
submitted to Physical Review Letters.

Talks related to the PhD thesis

1. **G. G. Kiss**, Gy. Gyürky, Z. Elekes, Zs. Fülöp, E. Somorjai, T. Rauscher and M. Wiescher,
Investigation of proton capture reaction cross sections on light p-nuclei,
Nuclear Physics in Astrophysics III., Dresden, Germany, 26 - 31 March 2007.
2. **G. G. Kiss**, Gy. Gyürky, A. Simon, Zs. Fülöp, E. Somorjai, T. Rauscher
Investigation of proton - induced reactions for the astrophysical p process,
Capture Gamma Ray and Related Topics XIII., Cologne, Germany, 25 - 29 August 2008.

Publications related to the astrophysical p process

1. Gy. Gyürky, Zs. Fülöp, **G. G. Kiss**, Z. Máté, E. Somorjai, J. Görres, A. Palumbo, M. Wiescher, D. Galaviz, A. Kretschmer, K. Sonnabend, A. Zilges and T. Rauscher,
A comprehensive study of the $^{106}Cd(\alpha,\gamma)^{110}Sn$ *reaction at energies relevant to the p process*,
Nuclear Physics A**758**, 517 (2004).
2. Gy. Gyürky, Z. Elekes, Zs. Fülöp, **G. G. Kiss**, E. Somorjai, A. Palumbo, M. Wiescher,
Precise half-life measurement of ^{110}Sn *and* ^{109}In *isotopes*,
Physical Review C **71**, 507302 (2005).

3. Gy. Gyürky, **G. G. Kiss**, Z. Elekes, Zs. Fülöp, E. Somorjai, A. Palumbo, J. Görres, H.-Y. Lee, W. Rapp, M. Wiescher, N. Özkan, R. T. Güray, G. Efe and T. Rauscher,
Alpha-induced cross sections of ^{106}*Cd for the astrophysical p process*,
Physical Review C **74**, 205805 (2006).

4. **G. G. Kiss**, Zs. Fülöp, Gy. Gyürky, Z. Máté, E. Somorjai, D. Galaviz, A. Kretschmer, K. sonnabend and A. Zilges,
Study of the ^{106}*Cd*$(\alpha,\alpha)^{106}$*Cd scattering at energies relevant to the p process*,
European Physical Journal A **27**, 197 (2006).

5. Zs. Fülöp, D. Galaviz, Gy. Gyürky, **G. G. Kiss**, Z. Máté, P. Mohr, T. Rauscher, E. Somorjai and A. Zilges,
Elastic alpha scattering on proton rich nuclei at astrophysically relevant energies, AIP. Conference Proceedings **847**, 351 (2006).

6. **G. G. Kiss**, Gy. Gyürky, Zs. Fülöp, E. Somorjai, D. Galaviz, A. Kretschmer, K. Sonnabend, A. Zilges, P. Mohr and M. Avrigeanu,
Study of the ^{89}*Y*$(\alpha,\alpha)^{89}$*Y reaction close to the Coulomb barrier*,
Journal of Physics G **35**, 4037 (2008).

7. **G. G. Kiss**, Gy. Gyürky, Zs. Fülöp, E. Somorjai, D. Galaviz, A. Kretschmer, K. Sonnabend, A. Zilges, P. Mohr and M. Avrigeanu,
Test of global alpha nucleus optical potentials with low energy ^{89}*Y*$(\alpha,\alpha)^{89}$*Y elastic scattering experiment*,
in preparation

Talks related to the astrophysical *p* process

1. **G. G. Kiss**, Gy. Gyürky, Zs. Fülöp, E. Somorjai, D. Galaviz, A. Kretschmer, K. Sonnabend, A. Zilges, P. Mohr and M. Avrigeanu,
Experimental study of the variation of alpha elastic scattering cross sections along isotopic and isotonic chains at low energies,

10th International Symposium on Origin of Matter and Evolution of Galaxies, Sapporo, Japan, 4 - 7 December (2007).

2. **G. G. Kiss**, Gy. Gyürky, Zs. Fülöp, E. Somorjai
   Elastic alpha scattering and alpha - nucleus optical potentials (in Hungarian)
   Magfizikus találkozó, Jávorkút 5 - 7 Május (2006).

Other publications

1. Gy. Gyürky, Zs. Fülöp, E. Somorjai, **G. G. Kiss** and C. Rolfs,
   Absolute resonance strengths in the $^{6,7}Li(\alpha,\gamma)^{10,11}B$ *reactions.*
   European Physical Journal **21**, 355 (2004).
2. A. Tumino, C. Spitaleri, A. M. Mukhamedzhanov, G. G. Rapisarda, S. Cherubini, V. Crucillá. Z. Elekes, Zs. Fülöp, M. Gulino, Gy. Gyürky, **G. G. Kiss**, M. La Cognata, L. Lamia, F. Mudó, R. G. Pizzone, S. Romano, M. L. Sergi and E. Somorjai,
   Supression of Coulomb interaction in the off - energy - shell p - p scattering from the p + d -> p + p + n reaction,
   Physical Review Letters **98**, 2502502 (2006).
3. A. Tumino, C. Spitaleri, G. G. Rapisarda, S. Cherubini, S. Blagus, M. Bogovac, V. Crucillá, Z. Elekes, Zs. Fülöp, M. Gulino, Gy. Gyürky, **G. G. Kiss**, M. La Cognata, L. Lamia, D. Miljanic, M. Milin, F. Mudó, A. M. Mukhamedzhanov, R. G. Pizzone, D. Rendic, S. Romano, M. L. Sergi and E. Somorjai,
   No signature of nuclear - Coulomb interference in the proton - proton elastic scattering via the Trojan Horse Method,
   Nuclear Physics A **787**, 337 (2007).
4. S. Romano, C. Spitaleri, S. Cherubini, V. Crucillá, M. Gulino, M. La Cognata, L. Lamia, R. G. Pizzone, S. M. R. Puglia, G. G. Rapisarda, M. L. Sergi, S Tudisco, A. Tumino, R. Tribble,

V. Goldberg, A. Mukhamedzhanov, G. Tabacaru, L. Trache, V. Kroha, V. Burian, Z. Hons, J. Novác, J. Vincour E. Somorjai, Z. Elekes, Gy. Gyürky, Zs. Fülöp, **G. G. Kiss**, A. Szánto de Toledo, N. Carlin, M. M. De Moura, M. G. Del Sánto, M. G. Munhoy, R. Liguori Neto, F. A. Souya, A. A. P. Suaide and E. Szánto,
The Trojan horse method in nuclear astrophysics,
Journal of Physics G **35**, 4008 (2008).

5. A. Tumino, C. Spitaleri, S. Cherubini, V. crucillá, Changbo Fu, Z. Elekes, Zs. Fülöp, V. Goldberg, M. Gulino, Gy. Gyürky, **G. G. Kiss**, M. La Cognata, L. Lamia, A. M. Mukhamedzhanov, R. G. Pizzone, S. M. R. Puglia, G. G. Rapisarda, C. Rolfs, S. Romano, M. L. Sergi, E. Somorjai, G. Tabacaru, L. Tracheand and R. Tribble,
The Trojan Horse Method as indirect technique in nuclear astrophysics,
Journal of Physics, Conference Series **111**, 012033 (2008).

Proton induced reactions and the astrophysical p process

Érrtekezés a doktori (Ph.D.) fokozat megszerzése érdekében a fizika tudományágban

Írta: Kiss Gábor Gyula okleveles fizikus

Készült a Debreceni Egyetem fizika tudományok doktori iskola magfizika programja keretében a Magyar Tudományos Akadémia Atommagkutató Intézetében

Témavezetõ: Dr. Somorjai Endre

Konzulens: Dr. Gyürky György

A doktori szigorlati bizottság:

elnök: Dr. ....
tagok: Dr. ....
Dr. ....

A doktori szigorlat idõpontja: 200.....................

A értekezés bírálói:

Dr. ....
Dr ....

A bírálóbizottság:

elnök: Dr. ....
tagok: Dr. ....
Dr. ....
Dr. ....
Dr. ....

Az értekezés védésének idõpontja: 200.....................